An *hp*-adaptive discontinuous Galerkin finite-element method for 3-D elastic wave modelling

V. Etienne,[1] E. Chaljub,[2] J. Virieux[2] and N. Glinsky[3,4]

[1]*Géoazur - Université de Nice Sophia-Antipolis - CNRS, France. E-mail: etienne@geoazur.unice.fr*
[2]*Laboratoire de Géophysique Interne et Tectonophysique - Université Joseph Fourier - CNRS, France*
[3]*LCPC/CETE de Nice, France*
[4]*INRIA Sophia Antipolis Méditerannée, France*

SUMMARY

We present a discontinuous Galerkin finite-element method (DG-FEM) formulation with Convolutional Perfectly Matched Layer (CPML) absorbing boundary condition for 3-D elastic seismic wave modelling. This method makes use of unstructured tetrahedral meshes locally refined according to the medium properties (*h*-adaptivity), and of approximation orders that can change from one element to another according to an adequate criterion (*p*-adaptivity). These two features allow us to significantly reduce the computational cost of the simulations. Moreover, we have designed an efficient CPML absorbing boundary condition, both in terms of absorption and computational cost, by combining approximation orders in the numerical domain. A quadratic interpolation is typically used in the medium to obtain the required accuracy, while lower approximation orders are used in the CPMLs to reduce the total computational cost and to obtain a well-balanced workload over the processors. While the efficiency of DG-FEMs have been largely demonstrated for high approximation orders, we favour the use of low approximation orders as they are more appropriate to the applications we are interested in. In particular, we address the issues of seismic modelling and seismic imaging in cases of complex geological structures that require a fine discretization of the medium. We illustrate the efficiency of our approach within the framework of the EUROSEISTEST verification and validation project, which is designed to compare high-frequency (up to 4 Hz) numerical predictions of ground motion in the Volvi basin (Greece). Through the tetrahedral meshing, we have achieved fine discretization of the basin, which appears to be a *sine qua non* condition for accurate computation of surface waves diffracted at the basin edges. We compare our results with predictions computed with the spectral element method (SEM), and demonstrate that our method yields the same level of accuracy with computation times of the same order of magnitude.

Key words: Surface waves and free oscillations; Site effects; Computational seismology; Wave propagation.

GJI Seismology

1 INTRODUCTION

Over the last decades, simulations of wave propagation in complex media have been efficiently tackled with finite-difference methods (FDMs) and applied with success to numerous physical problems (Graves 1996; Moczo *et al.* 2007). Nevertheless, FDMs suffer from some critical issues that are inherent to the underlying Cartesian grid, such as parasite diffractions in cases where the boundaries have a complex topography. To reduce these artefacts, the discretization should be fine enough to reduce the 'stair-case' effect at the free surface. For instance, a second-order rotated FDM requires up to 60 gridpoints per wavelength to compute an accurate seismic wavefield in elastic media with a complex topography (Bohlen &

Saenger 2006). Such constraints on the discretization drastically restrict the possible field of realistic applications. Some interesting combinations of FDMs and finite-element methods (FEMs) might overcome these limitations (Galis *et al.* 2008). The idea is to use an unstructured FEM scheme to represent both the topography and the shallow part of the medium, and to adopt for the rest of the model a classical FDM regular grid. For the same reasons as the issues related to the topography, uniform grids are not suitable for highly heterogeneous media, since the grid size is determined by the shortest wavelength. Except in some circumstances, like mixing grids (Aoi & Fujiwara 1999) or using non uniform Cartesian grids (Pitarka 1999) in the case of a low velocity layer, it is almost impossible to locally adapt the grid size to the medium properties in the

general case. From this point of view, FEMs are appealing, since they can use unstructured grids or meshes. Due to ever-increasing computational power, these kinds of methods have been the focus of a lot of interest and have been used intensively in seismology (Aagaard *et al.* 2001; Akcelik *et al.* 2003; Ichimura *et al.* 2007). Usually, the approximation order remains low, due to the prohibitive computational cost related to a non-diagonal mass matrix. However, this high computational cost can be avoided by mass lumping, a standard technique that replaces the large linear system by a diagonal matrix (Marfurt 1984; Chin-Joe-Kong *et al.* 1999). Another class of FEMs that relies on the Gauss–Lobatto–Legendre quadrature points has removed these limitations, and allows for spectral convergence with high approximation orders. This high-order FEM, called the spectral element method (SEM, Seriani & Priolo 1994; Komatitsch & Vilotte 1998), has been applied to large-scale geological models, up to the global scale (Chaljub *et al.* 2007; Komatitsch *et al.* 2008). The major limitation of SEM is the exclusive use of hexahedral meshes, which makes the design of an optimal mesh cumbersome in contrast to the flexibility offered by tetrahedral meshes. With tetrahedral meshes (Frey & George 2008), it is possible to fit almost perfectly complex topographies or geological discontinuities and the mesh width can be adapted locally to the medium properties (*h*-adaptivity). The extension of the SEM to tetrahedral elements represents ongoing work, while some studies have been done in two dimensions on triangular meshes (Mercerat *et al.* 2006; Pasquetti & Rapetti 2006). On the other hand, another kind of FEM has been proven to give accurate results on tetrahedral meshes: the discontinuous Galerkin finite-element method (DG-FEM) in combination with the arbitrary high-order derivatives (ADER) time integration (Dumbser & Käser 2006). Originally, DG-FEM was developed for the neutron transport equation (Reed & Hill 1973). It has been applied to a wide range of applications such as electromagnetics (Cockburn *et al.* 2004), aeroacoustics (Toulopoulos & Ekaterinaris 2006) and plasma physics (Jacobs & Hesthaven 2006), just to cite a few examples. This method relies on the exchange of numerical fluxes between adjacent elements. Contrary to classical FEMs, no continuity of the basis functions is imposed between elements, and therefore the method supports discontinuities in the seismic wavefield, as in the case of a fluid–solid interface. In such cases, the DG-FEM allows the same equation to be used for both the elastic and the acoustic media, and it does not require any explicit conditions on the interface (Käser & Dumbser 2008), which is, on the contrary, mandatory for continuous formulations, like the SEM (Chaljub *et al.* 2003). Moreover, the DG-FEM is completely local, which means that elements do not share their nodal values, contrary to conventional continuous FEM. Local operators make the method suitable for parallelization and allow for the mixing of different approximation orders (*p*-adaptivity).

However, in most studies, the DG-FEM is generally used with high approximation orders. Here, we present a low-order DG-FEM formulation with the convolutional perfectly matched layer (CPML) absorbing boundary condition (Roden & Gedney 2000; Komatitsch & Martin 2007) that is suitable for large-scale 3-D seismic wave simulations. In this context, the DG-FEM provides major benefits. Our approach relies intensively on the *p*-adaptivity. This last feature is crucial for efficient simulations, in order to mitigate the effects of the very small elements that are generally encountered in refined tetrahedral meshes. Indeed, the *p*-adaptivity allows an optimized time stepping to be achieved, by adapting the approximation order according to the size of the elements and the properties of the medium. The benefit of such a numerical scheme is particularly important with strongly heterogeneous media. Due to the mathematical

formulation we consider, the medium properties are assumed to be constant per element. Therefore, meshes have to be designed in such a way that this assumption is compatible with the expected accuracy. In particular, we address the issues of seismic modelling and seismic imaging in complex media. In the first application, the discretization must be able to represent the geological structures fairly, without oversampling, while in the second, the spatial resolution of the imaging process puts constraints on the coarsest parametrization of the medium. If we consider full waveform inversion (FWI) applications, the expected imaging resolution reaches half a wavelength, as shown by Sirgue & Pratt (2004). Therefore, following the Shannon theorem, a minimum number of four points per wavelength is required to obtain such accuracy. These reasons have motivated our development of DG-FEM with low orders. In this study, we focus on the quadratic interpolation, which yields a good compromise between accuracy, discretization and computational cost.

This paper is structured as follows. In Section 2, we review in detail the DG-FEM formulation, and introduce the concept of *p*-adaptivity. The implementation of the method on distributed memory machines is discussed in Section 3. The source excitation and two kinds of boundary conditions are explained in Section 4: the free surface, and the absorbing boundary conditions. Special attention is paid to the latter with the detailed CPML formulation. The efficiency of the CPML is demonstrated with validation tests that in some cases reveal instabilities inside the absorbing layers. The strategy for saving CPU time and memory with low-order CPML is then presented. In Section 5, we study the convergence of the method, and the ability to compute accurate surface waves when a free surface is considered. The advantages of the *hp*-adaptivity in the context of tetrahedral meshes are discussed in Section 6. Finally, in Section 7, we illustrate the efficiency of our method, with a challenging seismological model, where the computation of surface waves is critical for the prediction of site effects.

2 THE DG-FEM FORMULATION

2.1 Elastodynamic system

The equations governing particle velocity and stress in an isotropic elastic medium, namely the elastodynamic system (Virieux 1986), is a first-order hyperbolic system. Following the approach of BenJemaa *et al.* (2009), the elastodynamic system can be written in the following pseudo-conservative form

$$
\rho \partial_t \vec{v} = \sum_{\theta \in \{x,y,z\}} \partial_\theta (\mathcal{M}_\theta \vec{\sigma}) + \vec{f}
$$
$$
\Lambda \partial_t \vec{\sigma} = \sum_{\theta \in \{x,y,z\}} \partial_\theta (\mathcal{N}_\theta \vec{v}) + \Lambda \partial_t \vec{\sigma}_0,
\tag{1}
$$

with the definitions of the velocity and stress vectors as

$$
\vec{v} = (v_x \; v_y \; v_z)^T
$$
$$
\vec{\sigma} = (\tau \; \tau' \; \tau'' \; \sigma_{xy} \; \sigma_{xz} \; \sigma_{yz})^T,
\tag{2}
$$

and

$$
\tau = \frac{1}{3}(\sigma_{xx} + \sigma_{yy} + \sigma_{zz})
$$
$$
\tau' = \frac{1}{3}(2\sigma_{xx} - \sigma_{yy} - \sigma_{zz})
$$
$$
\tau'' = \frac{1}{3}(-\sigma_{xx} + 2\sigma_{yy} - \sigma_{zz}).
\tag{3}
$$

Due to the change of variables defined in eq. (3), the right-hand side of (1) does not include any terms that relate to the physical

properties. $\mathcal{M}_\theta$ and $\mathcal{N}_\theta$ are constant real matrices (Appendix B). Λ is a diagonal matrix given by

$$\Lambda = \text{diag}\left(\frac{3}{3\lambda + 2\mu}, \frac{3}{2\mu}, \frac{3}{2\mu}, \frac{1}{\mu}, \frac{1}{\mu}, \frac{1}{\mu}\right),$$

where λ and μ are the Lamé parameters. Moreover, the diagonality of Λ is an essential point of our formulation since the inverse of this matrix is required for the computation of the stress components (eq. 1). The extension of the pseudo-conservative form for the anisotropic or viscoelastic cases should be further analysed since the change of variable may depend on the physical parameters while the isotropic purely elastic case requires the simple global change of variables as shown in this study. Finally, in eq. (1), ρ is the medium density, while $\vec{f}$ and $\vec{\sigma}_0$ are the external forces and the initial stresses, respectively.

2.2 Spatial discretization

As is usual with FEMs (Zienkiewicz *et al.* 2005), we want to approximate the solution of eq. (1) by means of polynomial basis functions defined in volume elements. The spatial discretization is carried out with non-overlapping and conforming tetrahedra. We adopt the nodal form of the DG-FEM formulation (Hesthaven & Warburton 2008), assuming that the stress and velocity vectors are approximated in the tetrahedral elements as follows

$$\widehat{\vec{v}}_i(\vec{x}, t) = \sum_{j=1}^{d_i} \vec{v}_{ij}(\vec{x}_j, t)\, \varphi_{ij}(\vec{x})$$

$$\widehat{\vec{\sigma}}_i(\vec{x}, t) = \sum_{j=1}^{d_i} \vec{\sigma}_{ij}(\vec{x}_j, t)\, \varphi_{ij}(\vec{x}), \tag{4}$$

where i is the index of the element, $\vec{x}$ is the spatial coordinates inside the element, and t is the time. d_i is the number of nodes or degrees of freedom (DOF) associated with the interpolating Lagrangian polynomial basis function φ_{ij} relative to the jth node located at position $\vec{x}_j$. The expressions of the Lagrangian basis functions are given in Appendix A. $\vec{v}_{ij}$ and $\vec{\sigma}_{ij}$ are the velocity and stress vectors, respectively, evaluated at the jth node of the element. Although it is not an intrinsic limitation, we have adopted here the same set of basis functions for the interpolation of the velocity and the stress components. In the following, the notation P_k refers to a spatial discretization based on polynomial basis functions of degree k, and a P_k element is a tetrahedron in which a P_k scheme is applied. The number of DOF in a tetrahedral element is given by $d_i = (k + 1)(k + 2)(k + 3)/6$. For instance, in a P_0 element (Fig. 1a),

there is only one DOF (the stress and velocity are constant per element), while in a P_1 element (Fig. 1b), there are four DOF located at the four vertices of the tetrahedron (the stress and velocity are linearly interpolated). It is worth noting that the P_0 scheme corresponds to the case of the finite-volume method (BenJemaa *et al.* 2007, 2009; Brossier *et al.* 2008). For the quadratic approximation order P_2, one node is added at the middle of each edge of the tetrahedron, leading to a total of 10 DOF per element (Fig. 1c).

The first step in the finite-element formulation is to obtain the weak form of the elastodynamic system. To do so, we multiply eq. (1) by a test function φ_{ir} and integrate the system over the volume of the element i. For the test function, we adopt the same kind of function as used for the approximation of the solution. This case corresponds to the standard Galerkin method and can be written as

$$\int_{V_i} \varphi_{ir}\, \rho \partial_t \vec{v}\, \mathrm{d}V = \int_{V_i} \varphi_{ir} \sum_{\theta \in \{x,y,z\}} \partial_\theta (\mathcal{M}_\theta \vec{\sigma})\, \mathrm{d}V$$

$$\int_{V_i} \varphi_{ir}\, \Lambda \partial_t \vec{\sigma}\, \mathrm{d}V = \int_{V_i} \varphi_{ir} \sum_{\theta \in \{x,y,z\}} \partial_\theta (\mathcal{N}_\theta \vec{v})\, \mathrm{d}V \quad \forall r \in [1, \, d_i], \tag{5}$$

where V_i is the volume of the tetrahedral element i. For the purpose of clarity, we have omitted the external forces and stresses in (5). Integration by parts of the right-hand side of (5) leads to

$$\int_{V_i} \varphi_{ir}\, \rho \partial_t \vec{v}\, \mathrm{d}V = -\int_{V_i} \sum_{\theta \in \{x,y,z\}} \partial_\theta \varphi_{ir}\, (\mathcal{M}_\theta \vec{\sigma})\, \mathrm{d}V$$

$$+ \int_{S_i} \varphi_{ir} \left(\sum_{\theta \in \{x,y,z\}} \mathcal{M}_\theta\, n_\theta \right) \vec{\sigma}\, \mathrm{d}S$$

$$\int_{V_i} \varphi_{ir}\, \Lambda \partial_t \vec{\sigma}\, \mathrm{d}V = -\int_{V_i} \sum_{\theta \in \{x,y,z\}} \partial_\theta \varphi_{ir}\, (\mathcal{N}_\theta \vec{v})\, \mathrm{d}V$$

$$+ \int_{S_i} \varphi_{ir} \left(\sum_{\theta \in \{x,y,z\}} \mathcal{N}_\theta\, n_\theta \right) \vec{v}\, \mathrm{d}S, \tag{6}$$

with S_i as the surface of the element i, and $\vec{n} = (n_x, n_y, n_z)^T$ as the outward pointing unit normal vector with respect to the surface S_i. In the second term of the right-hand side of eq. (6), the fluxes of the stress and velocity wavefields across the faces of the element i appear. For evaluation of these fluxes, we adopt the centred flux scheme for its non-dissipative property (Remaki 2000; BenJemaa *et al.* 2009; Delcourte *et al.* 2009). Using eq. (4) and assuming constant physical properties per element, eq. (6) can be approximated
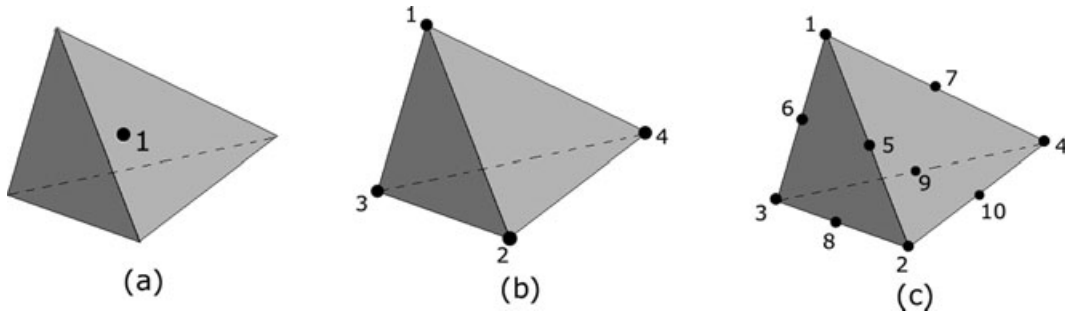

Figure 1. (a) P_0 element with one unique DOF. (b) P_1 element with four DOF. (c) P_2 element with 10 DOF.

with

$$\rho_i \int_{V_i} \varphi_{ir} \, \partial_t \widehat{\vec{v}}_i \, \mathrm{d}V = -\int_{V_i} \sum_{\theta \in \{x,y,z\}} \partial_\theta \varphi_{ir} \, (\mathcal{M}_\theta \widehat{\vec{\sigma}}_i) \, \mathrm{d}V$$

$$+ \frac{1}{2} \sum_{k \in N_i} \int_{S_{ik}} \varphi_{ir} \, \mathcal{P}_{ik} (\widehat{\vec{\sigma}}_i + \widehat{\vec{\sigma}}_k) \, \mathrm{d}S$$

$$\Lambda_i \int_{V_i} \varphi_{ir} \, \partial_t \widehat{\vec{\sigma}}_i \, \mathrm{d}V = -\int_{V_i} \sum_{\theta \in \{x,y,z\}} \partial_\theta \varphi_{ir} \, (\mathcal{N}_\theta \widehat{\vec{v}}_i) \, \mathrm{d}V$$

$$+ \frac{1}{2} \sum_{k \in N_i} \int_{S_{ik}} \varphi_{ir} \, \mathcal{Q}_{ik} (\widehat{\vec{v}}_i + \widehat{\vec{v}}_k) \, \mathrm{d}S, \qquad (7)$$

with $k \in N_i$ representing the elements k adjacent to the element i, and S_{ik} the face between elements i and k. $\mathcal{P}$ and $\mathcal{Q}$ are defined as follows

$$\mathcal{P}_{ik} = \sum_{\theta \in \{x,y,z\}} n_{ik\theta} \, \mathcal{M}_\theta$$

$$\mathcal{Q}_{ik} = \sum_{\theta \in \{x,y,z\}} n_{ik\theta} \, \mathcal{N}_\theta,$$

where $n_{ik\theta}$ is the component along the θ axis of the unit vector $\vec{n}_{ik}$ of the face S_{ik} that points from element i to element k. Eq. (7) indicates that the computations of the stress and velocity wavefields in one element require information from the directly neighbouring elements. This illustrates clearly the local nature of DG-FEM. Using the tensor product $\otimes$, we obtain the expression

$$\rho_i (\mathcal{I}_3 \otimes \mathcal{K}_i) \partial_t \vec{v}_i = - \sum_{\theta \in \{x,y,z\}} (\mathcal{M}_\theta \otimes \mathcal{E}_{i\theta}) \vec{\sigma}_i$$

$$+ \frac{1}{2} \sum_{k \in N_i} \left[(\mathcal{P}_{ik} \otimes \mathcal{F}_{ik}) \vec{\sigma}_i + (\mathcal{P}_{ik} \otimes \mathcal{G}_{ik}) \vec{\sigma}_k \right]$$

$$(\Lambda_i \otimes \mathcal{K}_i) \partial_t \vec{\sigma}_i = - \sum_{\theta \in \{x,y,z\}} (\mathcal{N}_\theta \otimes \mathcal{E}_{i\theta}) \vec{v}_i$$

$$+ \frac{1}{2} \sum_{k \in N_i} \left[(\mathcal{Q}_{ik} \otimes \mathcal{F}_{ik}) \vec{v}_i + (\mathcal{Q}_{ik} \otimes \mathcal{G}_{ik}) \vec{v}_k \right], \qquad (8)$$

where $\mathcal{I}_3$ represents the identity matrix. In eq. (8), the vectors $\vec{v}_i$ and $\vec{\sigma}_i$ should be read as the collection of all nodal values of the velocity and stress components in the element i. We now introduce the mass matrix

$$(\mathcal{K}_i)_{rj} = \int_{V_i} \varphi_{ir} \, \varphi_{ij} \, \mathrm{d}V \qquad j, r \in [1, d_i], \qquad (9)$$

the stiffness matrix

$$(\mathcal{E}_{i\theta})_{rj} = \int_{V_i} (\partial_\theta \varphi_{ir}) \, \varphi_{ij} \, \mathrm{d}V \qquad j, r \in [1, d_i], \qquad (10)$$

with $\theta \in \{x, y, z\}$, and the flux matrices

$$(\mathcal{F}_{ik})_{rj} = \int_{S_{ik}} \varphi_{ir} \, \varphi_{ij} \, \mathrm{d}S \qquad j, r \in [1, d_i] \qquad (11)$$

$$(\mathcal{G}_{ik})_{rj} = \int_{S_{ik}} \varphi_{ir} \, \varphi_{kj} \, \mathrm{d}S \qquad r \in [1, d_i] \qquad j \in [1, d_k]. \qquad (12)$$

It is worth noting that in eq. (12), the DOF of elements i and k appear (d_i and d_k, respectively) indicating that the approximation orders are totally decoupled from one element to another. Therefore, the DG-FEM allows for varying approximation orders in the numerical scheme. This feature is referred to as *p*-adaptivity. Moreover, given an approximation order, these matrices are unique for all elements (with a normalization according to the volume or surface of the

elements) and they can be computed before hand with appropriate integration quadrature rules. The memory requirement is therefore low, since only a collection of small matrices is needed according to the possible combinations of approximation orders. The maximum size of these matrices is $(d_{\max} \times d_{\max})$ where $d_{\max}$ is the maximum number of DOF per element and the number of matrices to store is given by the square of the number of approximation orders mixed in the numerical domain. Details regarding the computation of the matrices are given in Appendix B. It should be mentioned that to retrieve both the velocity and the stress components, eq. (8) requires the computation of $\mathcal{K}_i^{-1}$, which can also be performed before hand.

Note that if we want to consider variations in the physical properties inside the elements, the pseudo-conservative form makes the computation of flux much easier and computationally more efficient than in the classical elastodynamic system. These properties come from the fact that in the pseudo-conservative form, the physical properties are located in the left-hand side of eq. (1). Therefore, no modification of the stiffness and flux matrices nor additional terms are needed in eq. (8) to take into account the variation of properties. Only the mass matrix needs to be evaluated for each element and for each physical property according to the expression

$$(\mathcal{K}_i)_{rj} = \int_{V_i} \chi_i(\vec{x}) \, \varphi_{ir}(\vec{x}) \, \varphi_{ij}(\vec{x}) \, \mathrm{d}V \qquad j, r \in [1, d_i], \qquad (13)$$

where $\chi_i(\vec{x})$ represents the physical property (ρ_i or one of the Λ_i components) varying inside the element.

2.3 Time discretization

For the time integration of eq. (8), we adopt a second-order explicit leap-frog scheme that allows to compute alternatively the velocity and the stress components between a half time step. Eq. (8) can be written as

$$\rho_i (\mathcal{I}_3 \otimes \mathcal{K}_i) \frac{\vec{v}_i^{n+\frac{1}{2}} - \vec{v}_i^{n-\frac{1}{2}}}{\Delta t} = - \sum_{\theta \in \{x,y,z\}} (\mathcal{M}_\theta \otimes \mathcal{E}_{i\theta}) \vec{\sigma}_i^n$$

$$+ \frac{1}{2} \sum_{k \in N_i} \left[(\mathcal{P}_{ik} \otimes \mathcal{F}_{ik}) \vec{\sigma}_i^n + (\mathcal{P}_{ik} \otimes \mathcal{G}_{ik}) \vec{\sigma}_k^n \right]$$

$$(\Lambda_i \otimes \mathcal{K}_i) \frac{\vec{\sigma}_i^{n+1} - \vec{\sigma}_i^n}{\Delta t} = - \sum_{\theta \in \{x,y,z\}} (\mathcal{N}_\theta \otimes \mathcal{E}_{i\theta}) \vec{v}_i^{n+\frac{1}{2}}$$

$$+ \frac{1}{2} \sum_{k \in N_i} \left[(\mathcal{Q}_{ik} \otimes \mathcal{F}_{ik}) \vec{v}_i^{n+\frac{1}{2}} + (\mathcal{Q}_{ik} \otimes \mathcal{G}_{ik}) \vec{v}_k^{n+\frac{1}{2}} \right], \qquad (14)$$

where the superscript n indicates the time step. We chose to apply the definition of the time step as given by Käser *et al.* (2008), which links the mesh width and time step as follows

$$\Delta t < \min_i \left(\frac{1}{2k_i + 1} \cdot \frac{2r_i}{V_{P_i}} \right), \qquad (15)$$

where r_i is the radius of the sphere inscribed in the element indexed by i, V_{P_i} is the P-wave velocity in the element, and k_i is the polynomial degree used in the element. Eq. (15) is a heuristic stability criterion that usually works well. However, there is no mathematical proof for unstructured meshes that guarantees numerical stability.

3 COMPUTATIONAL ASPECTS

As mentioned in Section 2, the DG-FEM is a local method, and therefore it is naturally suitable for parallel computing. In our implementation, the parallelism relies on a domain-partitioning strategy, assigning one subdomain to one CPU. This corresponds to the
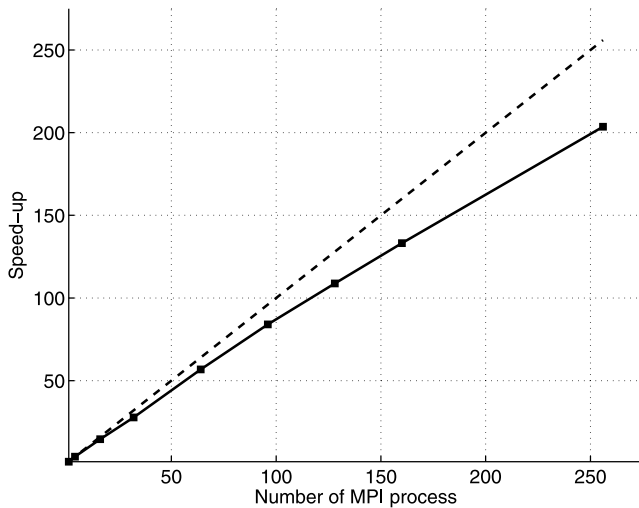
Figure 2. Speed-up observed when the number of MPI processes is increased from 1 to 256 for modelling with a mesh of 1.8 million P_2 elements. The ideal speed-up is plotted with a dashed line, the observed speed-up with a continuous line. These values were observed on a computing platform with bi-processor quad core Opteron 2.3 GHz CPUs interconnected with Infiniband at 20 Gb s^{-1}.

single program mutiple data (SPMD) architecture, which means that there is only one program and each CPU uses the same executable to work on different parts of the 3-D mesh. Communication between the subdomains is performed with the message passing interface (MPI) parallel environment (Aoyama & Nakano 1999), which allows for applications to run on distributed memory machines. For efficient load balancing among the CPUs, the mesh is divided with the partitioner METIS (Karypis & Kumar 1998), to balance the number of elements in the subdomains, and to minimize the number of adjacent elements between the subdomains. These two criteria are crucial for the efficiency of the parallelism on large-scale numerical simulations. Fig. 2 shows the observed speed-up (i.e. the ratio between the computation time with one CPU, and the computation time with N CPUs) when the number of MPI processes is increased from 1 to 256, for strong scaling calculations on a fixed mesh of 1.8 million P_2 elements. This figure shows good efficiency of the parallelism, of around 80 per cent.

In our formulation, another key point is the time step, which is common for all of the subdomains. The time step should satisfy the stability condition given in eq. (15) for every element. Consequently, the element with the smallest time step imposes its time step on all of the subdomains. We should mention here a more elaborate approach with local time stepping (Dumbser *et al.* 2007) that allows for elements to have their own time step independent of the others. Nevertheless, the *p*-adaptivity offered by DG-FEM allows mitigation of the computational burden resulting from the common time step. This point is detailed in section 6. From a technical point of view, we implemented the method in the FORTRAN 90 language without the use of specific mathematical libraries like Basic Linear Algebra Subroutines (BLAS). Indeed, the matrix products in the DG-FEM formulation involve relatively small matrices (typically 10×10 in P_2). Therefore, we did not experience substantial gains when calling mathematical libraries, as already observed by Komatitsch *et al.* (2008) for SEM.

4 SOURCE EXCITATION AND BOUNDARY CONDITIONS

We consider here the implementation of a point source in the DG-FEM, and we detail two types of boundary conditions that are generally encountered in seismic modelling: the free surface, and the absorbing boundary conditions. Special attention is given to the latter, based on the CPML (Drossaert & Giannopoulos 2007; Komatitsch & Martin 2007). To our knowedge, this point has not been studied intensely in a DG-FEM framework.

4.1 Source excitation

The excitation of a point source is projected onto the nodes of the element that contains the source as follows

$$\vec{s}_i^n = \frac{\vec{\varphi}_i(\vec{x}_s)}{\sum_{j=1}^{d_i} \varphi_{ij}(\vec{x}_s) \int_{V_i} \varphi_{ij}(\vec{x}) \mathrm{d}V} s(t), \tag{16}$$

with $\vec{s}_i^n$ the nodal values vector associated to the excited component, $t = n\Delta t$, $\vec{x}_s$ the position of the point source and $s(t)$ the source function. Eq. (16) gives the source term that should be added to the right-hand side of eq. (14) for the required components. It should be noticed that this term is only applied to the element containing the source. Depending on the approximation order, the spatial support of the source varies. Fig. 3(a) shows that the support of a P_0 element is actually the whole volume of the element (represented on the cross-section with a homogeneous white area). In this case, no precise localization of the source inside the element is possible due to the constant piecewise interpolation approximation. On the other hand, in a P_1 element (Fig. 3b), the spatial support of the source is linear and allows for a rough localization of the source. In a P_2
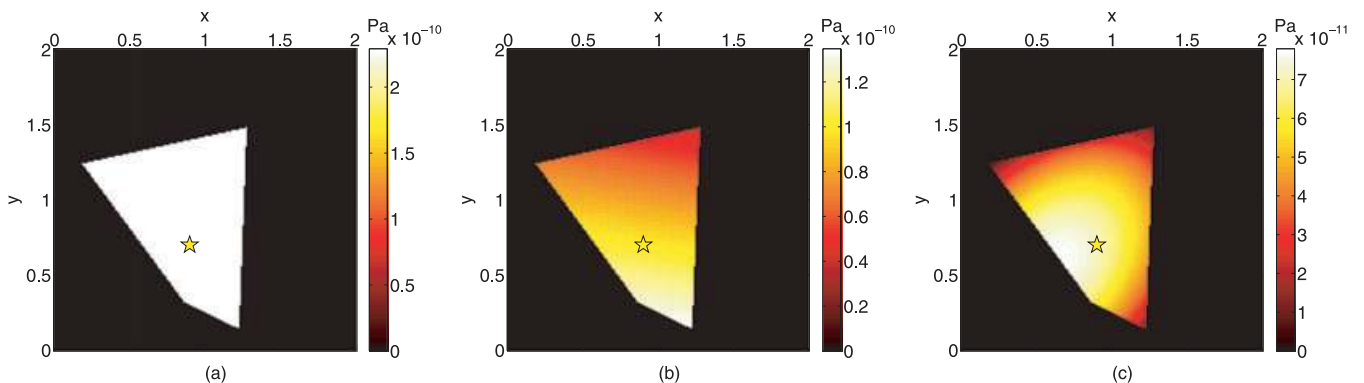

Figure 3. (a) Cross-section of the mesh near the source position, indicated with a yellow star in the *xy* plane. This view represents the spatial support of the stress component in a P_0 element containing the point source. (b) Same as (a) with a P_1 element. (c) Same as (a) with a P_2 element.

element (Fig. 3c), the quadratic spatial support tends to resemble the expected Dirac in space close to the source position. It should be noted that the limitations concerning source localization also apply to the solution extraction at the receivers, according to the approximation order of the elements containing the receivers.

4.2 Free surface condition

For the element faces located on the free surface, we use an explicit condition by changing the flux expression locally. This is carried out with the concept of virtual elements, which are exactly symmetric to the elements located on the free surface. Inside the virtual elements, we impose a velocity wavefield that is identical to the wavefield of the corresponding inner elements, and we impose an opposite stress wavefield. As a result, the velocity is seen as continuous across the free surface, while the stress is equal to zero on the faces related to the free surface.

4.3 Absorbing boundary condition

For simulations in an infinite medium, an absorbing boundary condition needs to be applied at the edges of the numerical model. An efficient way to mimic such an infinite medium can be achieved with PMLs, which was initially developed by Berenger (1994) for electromagnetics, and adapted for elastodynamics by Chew & Liu (1996). PMLs are anisotropic absorbing layers that are added at the periphery of the numerical model. The classical PML formulation is based on splitting of the elastodynamic equations. In the following, we use a new kind of PML, known as CPML, which does not require split terms. The CPML originated from Roden & Gedney (2000) for electromagnetics and was applied by Komatitsch & Martin (2007) and Drossaert & Giannopoulos (2007) to the elastodynamic system. CPML is based on an idea of Kuzuoglu & Mittra (1996), who obtained a strictly causal form of PML by adding some parameters in the standard damping function of Berenger (1994), which enhanced the absorption of waves arriving at the boundaries of the model with grazing incidence angles.

4.3.1 CPML formulation

Inside the CPML, a damping function is applied only onto the spatial derivative perpendicular to the boundary. In the CPML formulation, the damping function is defined in the frequency domain as follows

$$s_\theta = \kappa_\theta + \frac{d_\theta}{\alpha_\theta + i\omega} \qquad \forall \theta \in \{x, y, z\}, \tag{17}$$

with angular frequency ω and coefficients $\kappa_\theta \geq 1$ and $\alpha_\theta \geq 0$. The damping profile d_θ varies from 0 at the entrance of the layer, up to a maximum real value $d_{\theta max}$ at the end (Collino & Tsogka 2001) such that

$$d_\theta = d_{\theta max} \left(\frac{\delta_\theta}{L_{cpml}} \right)^2, \tag{18}$$

and

$$d_{\theta max} = -3V_P \frac{\log(R_{coeff})}{2L_{cpml}} \qquad \forall \theta \in \{x, y, z\}, \tag{19}$$

with δ_θ as the depth of the element barycentre inside the CPML, L_{cpml} the thickness of the absorbing layer, and R_{coeff} the theoretical reflection coefficient. For all of the tests presented in the following, we chose $R_{coeff} = 0.1$ per cent. α_θ is a coefficient that varies from a maximum value ($\alpha_{\theta max} = \pi f_0$) at the entrance of the CPML, to zero

at its end. If $\kappa_\theta = 1$ and $\alpha_\theta = 0$, the classical PML formulation is obtained. In the CPML, the spatial derivatives are replaced by

$$\partial_{\tilde\theta} \to \frac{1}{\kappa_\theta} \partial_\theta + \zeta_\theta * \partial_\theta \qquad \forall \theta \in \{x, y, z\}, \tag{20}$$

with

$$\zeta_\theta(t) = -\frac{d_\theta}{\kappa_\theta^2} H(t) e^{-(d_\theta \kappa_\theta + \alpha_\theta)t} \qquad \forall \theta \in \{x, y, z\}, \tag{21}$$

where *H(t)* denotes the Heaviside distribution. Roden & Gedney (2000) have demonstrated that the time convolution in eq. (20) can be performed in a recursive way using memory variables defined by

$$\psi_\theta = \zeta_\theta * \partial_\theta \qquad \forall \theta \in \{x, y, z\}. \tag{22}$$

ψ_θ represents a memory variable in the sense that it is updated at each time step. Komatitsch & Martin (2007) showed that the term κ_θ has a negligible effect on the absorbing abilities, and it can be set to 1. If we take $\kappa_\theta = 1$ and derive eq. (22) using eq. (21), we get

$$\partial_t \psi_\theta = -d_\theta \partial_\theta - (d_\theta + \alpha_\theta)\psi_\theta \qquad \forall \theta \in \{x, y, z\}. \tag{23}$$

We can introduce the memory variables into the initial elastodynamic system of eq. (1) with the definition of vectors

$$\vec{\psi}_\theta(\vec{v}) = [\psi_\theta(v_x)\ \psi_\theta(v_y)\ \psi_\theta(v_z)]^T$$
$$\vec{\psi}_\theta(\vec{\sigma}) = [\psi_\theta(\tau)\ \psi_\theta(\tau')\ \psi_\theta(\tau'')\ \psi_\theta(\sigma_{xy})\ \psi_\theta(\sigma_{xz})\ \psi_\theta(\sigma_{yz})]^T$$
$$\forall \theta \in \{x, y, z\}. \tag{24}$$

If we apply the change of variables in eq. (20), eq. (1) becomes

$$\rho \partial_t \vec{v} = \sum_{\theta \in \{x,y,z\}} \partial_\theta (\mathcal{M}_\theta \vec{\sigma}) + \sum_{\theta \in \{x,y,z\}} \mathcal{M}_\theta \vec{\psi}_\theta(\vec{\sigma})$$
$$\Lambda \partial_t \vec{\sigma} = \sum_{\theta \in \{x,y,z\}} \partial_\theta (\mathcal{N}_\theta \vec{v}) + \sum_{\theta \in \{x,y,z\}} \mathcal{N}_\theta \vec{\psi}_\theta(\vec{v}). \tag{25}$$

Eq. (25) is the initial elastodynamic system augmented by the memory variables on the right-hand side. In combination, another extra system dealing with the memory variables is

$$\partial_t \vec{\psi}_\theta(\vec{\sigma}) = -d_\theta \partial_\theta(\vec{\sigma}) - (d_\theta + \alpha_\theta)\vec{\psi}_\theta(\vec{\sigma})$$
$$\partial_t \vec{\psi}_\theta(\vec{v}) = -d_\theta \partial_\theta(\vec{v}) - (d_\theta + \alpha_\theta)\vec{\psi}_\theta(\vec{v}) \quad \forall \theta \in \{x, y, z\}. \tag{26}$$

The collection of memory variables associated with each element located in the CPMLs is made of 22 memory variables per DOF. These variables correspond to the 22 spatial derivatives involved in eq. (1). If we apply the DG-FEM formulation as presented in the previous section to eqs (25) and (26), we get

$$\rho_i (\mathcal{I}_3 \otimes \mathcal{K}_i) \frac{\vec{v}_i^{n+\frac{1}{2}} - \vec{v}_i^{n-\frac{1}{2}}}{\Delta t} = - \sum_{\theta \in \{x,y,z\}} (\mathcal{M}_\theta \otimes \mathcal{E}_{i\theta})\vec{\sigma}_i^n$$

$$+ \frac{1}{2} \sum_{k \in N_i} \left[(\mathcal{P}_{ik} \otimes \mathcal{F}_{ik})\vec{\sigma}_i^n + (\mathcal{P}_{ik} \otimes \mathcal{G}_{ik})\vec{\sigma}_k^n \right]$$

$$+ (\mathcal{I}_3 \otimes \mathcal{K}_i) \sum_{\theta \in \{x,y,z\}} \mathcal{M}_\theta \vec{\psi}_\theta \left(\vec{\sigma}_i^n \right)$$

$$(\Lambda_i \otimes \mathcal{K}_i) \frac{\vec{\sigma}_i^{n+1} - \vec{\sigma}_i^n}{\Delta t} = - \sum_{\theta \in \{x,y,z\}} (\mathcal{N}_\theta \otimes \mathcal{E}_{i\theta})\vec{v}_i^{n+\frac{1}{2}}$$

$$+ \frac{1}{2} \sum_{k \in N_i} \left[(\mathcal{Q}_{ik} \otimes \mathcal{F}_{ik})\vec{v}_i^{n+\frac{1}{2}} + (\mathcal{Q}_{ik} \otimes \mathcal{G}_{ik})\vec{v}_k^{n+\frac{1}{2}} \right]$$

$$+ (\mathcal{I}_3 \otimes \mathcal{K}_i) \sum_{\theta \in \{x,y,z\}} \mathcal{N}_\theta \vec{\psi}_\theta \left(\vec{v}_i^{n+\frac{1}{2}} \right), \tag{27}$$

incombination with the memory-variable system

$$(\mathcal{I}_3 \otimes \mathcal{K}_i)\frac{\vec{\psi}_\theta\left(\vec{\sigma}_i^n\right) - \vec{\psi}_\theta\left(\vec{\sigma}_i^{n-1}\right)}{\Delta t} = d_{i\theta}(\mathcal{I}_6 \otimes \mathcal{E}_{i\theta})\vec{\sigma}_i^{n-1}$$

$$- d_{i\theta}\frac{1}{2}\sum_{k \in N_i} n_{ik\theta}\left[(\mathcal{I}_6 \otimes \mathcal{F}_{ik})\vec{\sigma}_i^{n-1} + (\mathcal{I}_6 \otimes \mathcal{G}_{ik})\vec{\sigma}_k^{n-1}\right]$$

$$- (\mathcal{I}_3 \otimes \mathcal{K}_i)(d_{i\theta} + \alpha_{i\theta})\vec{\psi}_\theta\left(\vec{\sigma}_i^{n-1}\right)$$

$$(\mathcal{I}_3 \otimes \mathcal{K}_i)\frac{\vec{\psi}_\theta\left(\vec{v}_i^{n+\frac{1}{2}}\right) - \vec{\psi}_\theta\left(\vec{v}_i^{n-\frac{1}{2}}\right)}{\Delta t} = \sum_{\theta \in \{x,y,z\}} d_{i\theta}(\mathcal{I}_3 \otimes \mathcal{E}_{i\theta})\vec{v}_i^{n-\frac{1}{2}}$$

$$- d_{i\theta}\frac{1}{2}\sum_{k \in N_i} n_{ik\theta}\left[(\mathcal{I}_3 \otimes \mathcal{F}_{ik})\vec{v}_i^{n-\frac{1}{2}} + (\mathcal{I}_3 \otimes \mathcal{G}_{ik})\vec{v}_k^{n-\frac{1}{2}}\right]$$

$$- (\mathcal{I}_3 \otimes \mathcal{K}_i)(d_{i\theta} + \alpha_{i\theta})\vec{\psi}_\theta\left(\vec{v}_i^{n-\frac{1}{2}}\right) \qquad \forall\theta \in \{x, y, z\}. \qquad (28)$$

Eqs (27) and (28) indicate that p-adaptivity is also supported in the CPMLs. At the end of the CPMLs, we apply a simple free surface condition as explained in the previous section.

4.3.2 Validation tests

To validate the efficiency of the CPML, we present some simulations of wave propagation in a homogeneous, isotropic and purely elastic medium. The model size is 8 km × 8 km × 8 km, and the medium properties are: $V_P = 4000 \text{ m s}^{-1}$, $V_S = 2310 \text{ m s}^{-1}$ and $\rho = 2000 \text{ kg m}^{-3}$. An explosive source is placed at coordinates ($x_s = 2000$ m, $y_s = 2000$ m, $z_s = 4000$ m) and a line of receivers is located at coordinates (3000 m ≤ x_r ≤ 6000 m, $y_r = 2000$ m, $z_r = 4000$ m) with 500 m between receivers. The conditions of the tests are particularly severe, since the source and the receivers are located close to the CPMLs (at a distance of 250 m), thus favouring grazing waves. The source signature is a Ricker wavelet with a dominant frequency of 3 Hz and a maximum frequency of about 7.5 Hz. Due to the explosive source, only P-wave is generated and the minimum wavelength is about 533 m. The mesh contains 945 477 tedrahedra with an average edge of 175 m, making a discretization of about 3 elements per $\lambda_{\min}$. Figs 4(c) and (d) show the results obtained with the P_2 interpolation and CPMLs of 10-elements width ($L_{\text{cpml}} = 1750$ m) at all edges of the model. With the standard scale, no reflection can be seen from the CPMLs. When the amplitude is magnified by a factor of 100, some spurious reflections are visible. This observation is in agreement with the theoretical reflection coefficient ($R_{\text{coeff}} = 0.1$ per cent) in eq. (19). Fig. 5(a) allows to compare the seismograms computed with CPMLs of 10-elements width and the seismograms computed in a larger model without reflection in the time window.

As shown by Collino & Tsogka (2001), the thickness of the absorbing layer plays an important role in the absorption efficiency. In Figs 4(a) and (b), the same test was performed with CPMLs of five-elements width ($L_{\text{cpml}} = 875$ m) at all edges of the model.
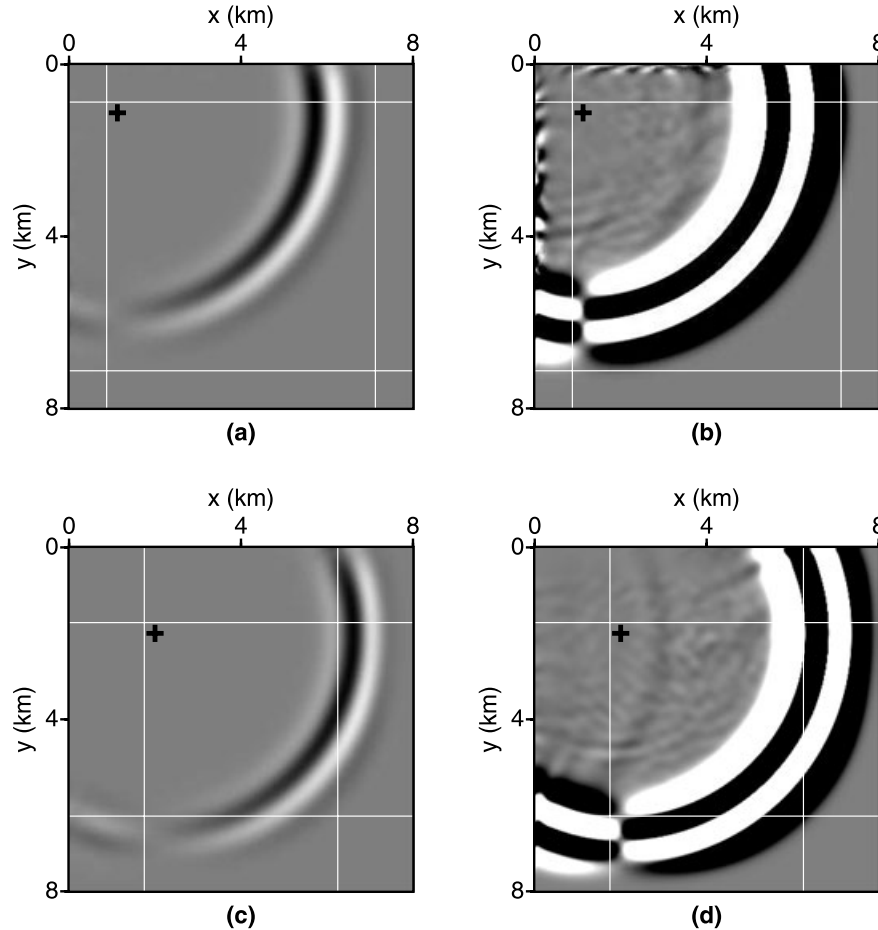

Figure 4. Snapshots at 1.6 s of the velocity component v_x in the plane xy that contains the source location. CPMLs of five-elements width are applied at all edges of the model. The modelling was carried out with P_2 interpolation. White lines, the limits of the CPMLs; black cross, the position of the source. (a) Real amplitude. (b) Amplitude magnified by a factor of 100. (c) and (d) Same as (a) and (b) with CPMLs of 10-elements width.
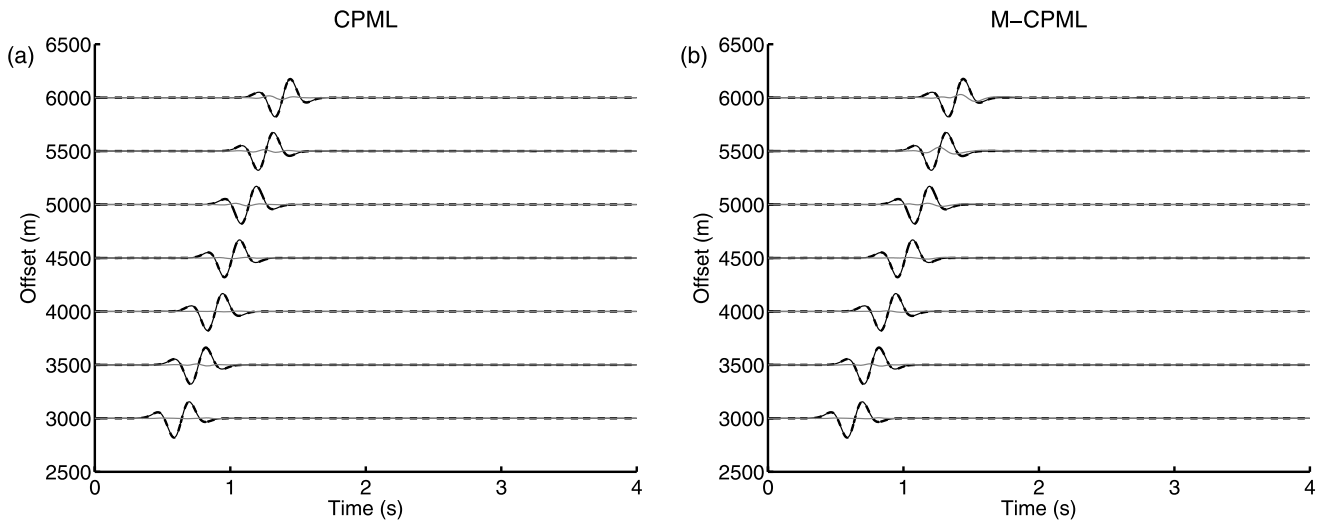
Figure 5. (a) Seismograms of the velocity component v_x. The amplitude of each seismogram is normalized. Black continuous line, numerical solution in large model without reflection in the time window; dashed line, numerical solution with 10-elements width CPMLs; grey line, residuals magnified by a factor of 10. (b) Same as (a) with 10-elements width M-CPMLs.

Compared to Figs 4(c) and (d), the amplitude of the reflections have the same order of magnitude. Nevertheless, in the upper and left parts of the model, some areas with a strong amplitude appear close to the edges. These numerical instabilities arise at the outer edges of the CPMLs, and they expand over the complete model during the simulations. Instabilities of PML in long time simulations have been studied in electromagnetics (Abarbanel *et al.* 2002; Bécache *et al.* 2004). In the following, we present a numerical stability study of CPML combined with DG-FEM for the elastodynamics. The results are shown in Fig. 6, with snapshots at long times for CPMLs of 5- and 10-elements widths. In these snapshots, the instabilities arise at the four corners of the model (at 20 s for the 10-elements width CPML). Tests with larger CPMLs (not shown) demonstrate that when the CPML width is 20 elements, these instabilities do not appear. Such instabilities were experienced by Meza-Fajardo & Papageorgiou (2008) with standard PML, for an isotropic medium. These authors proposed the application of an additional damping in the PML, onto the directions parallel to the layer, leading to a multiaxial PML (M-PML). Fig. 7 is equivalent to Fig. 6, instead that 10 per cent of the damping profile defined in eq. (18) has been added onto the directions parallel to the CPMLs (in the latter named M-CPMLs). As a result, instabilities do not appear when the CPML width is at least 10 elements while the efficiency of the absorption is preserved as shown by Fig. 5(b) with similar residuals compared to Fig. 5(a).

4.3.3 Saving computation time and memory

Table 1 gives the computation times for updating the velocity and stress wavefields in one element for one time step, for different approximation orders, without or with the update of the CPML memory variables (i.e. elements located outside or inside the CPMLs). These computation times illustrate the significant increase with respect to the approximation order, and they allow an evaluation of the additional costs of the CPML memory variables computation from 40 per cent to 60 per cent. The effects of this additionnal cost have to be analysed in the context of a domain-partitioning strategy. As introduced in Section 3, the mesh is divided into subdomains, using a partitioner. Fig. 8(a) shows the layout of the subdomains that were

obtained with the partitioner METIS (Karypis & Kumar 1998) along the *xy* plane used in the previous validation tests. The mesh was divided into 32 partitions, although only a few of these are visible on the cross-section in Fig. 8(a). We used an unweighted partitioning, meaning that each partition contains approximately the same number of elements. The subdomains, partially located in the CPMLs, contain different numbers of CPML elements. In large simulations, some subdomains are totally located inside the CPMLs, and some others outside the CPMLs. In such a case, the extra computation costs of the subdomains located in the absorbing layers penalize the whole simulation. Indeed, most of the subdomains spend 40–60 per cent of the time just waiting for the subdomains located in the CPMLs to complete the computations at each time step. For a better load balancing, we propose to benefit from the *p*-adaptivity of DG-FEM, using lower approximation orders in the CPMLs. Indeed, inside the absorbing layers, we do not need a specific accuracy, and consequently the approximation order can be decreased. Table 1 indicates that such a mixed numerical scheme is advantageous, since the computation time required for a P_0 or P_1 element located in the CPML is shorter than the computation time of a standard P_2 element. Fig. 8(b) shows the approximation order per element when P_1 is used in the CPMLs and P_2 in the rest of the medium. We should note here that the interface between these two areas is not strictly aligned to a cartesian axis, and has some irregularities due to the shape of the tetrahedra. Although it is possible to constrain the alignment of the element faces parallel to the CPML limits, we did not observe significant differences in the absorption efficiency whether the faces are aligned or not.

Fig. 9(a) shows the seismograms computed when the modelling was carried out with P_2 inside the medium and P_1 in the CPMLs. Absorbing layers of 10-elements width are applied at all edges of the model. For comparison, Fig. 9(b) shows the results obtained with P_0 in the CPMLs and P_2 for the rest of the medium. In this case, the spurious reflections have significant amplitudes. The snaphots (not presented here) reveal a large number of artefacts both in the CPMLs and in the medium. These artefacts make it impossible to use these seismograms for practical applications. On the other hand, the seismograms computed with the mixed scheme P_2/P_1 show weak artefacts, and are reasonably comparable with the
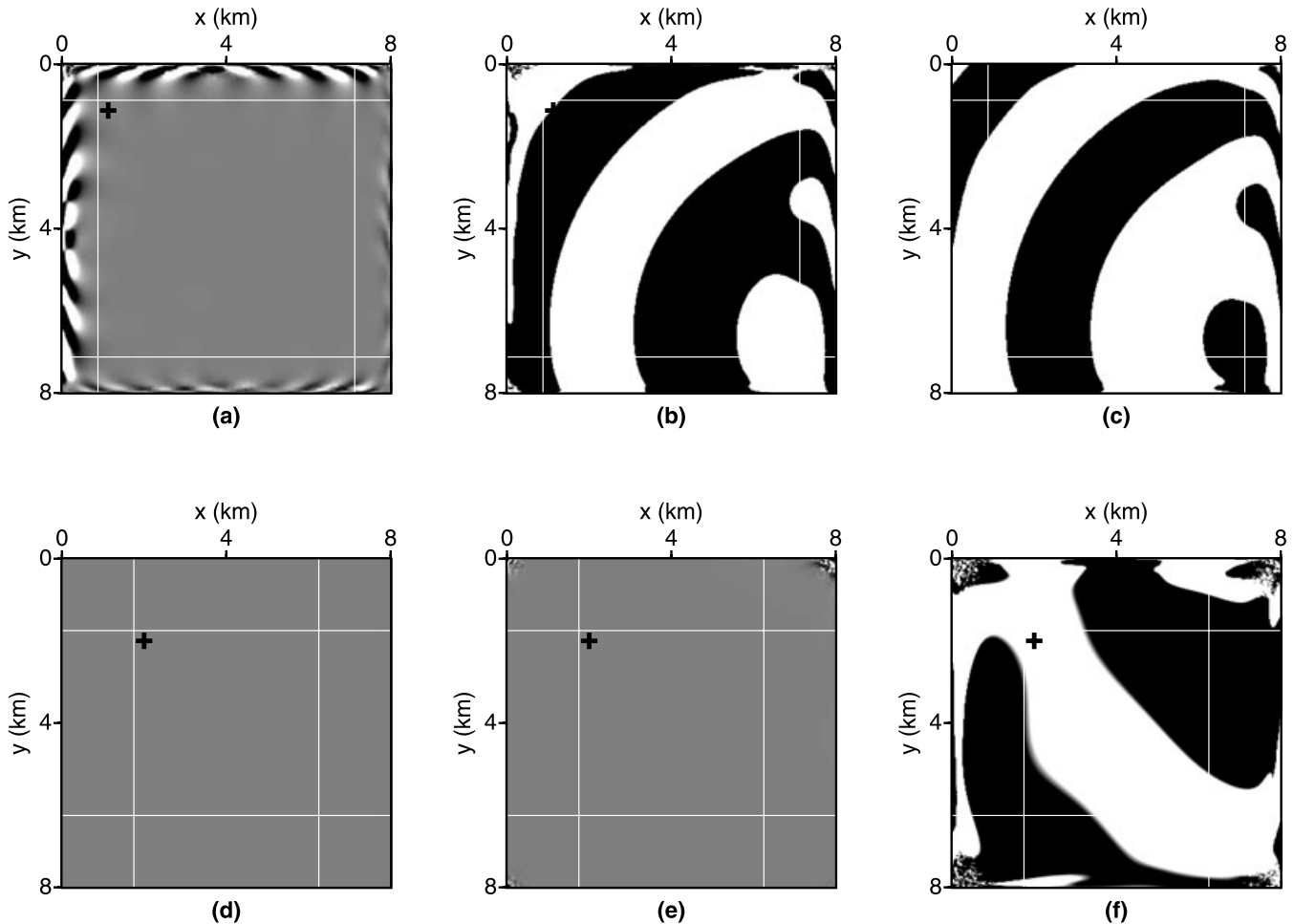
Figure 6. (a), (b) and (c) Snapshots of the velocity component v_x in the plane xy that contains the source location at 10, 20 and 30 s, respectively. The amplitude is plotted without any magnification factor. The modelling was carried out with P_2 interpolation. CPMLs with five-elements width are applied at all edges of the model. White lines, the limits of the CPMLs; black cross, the position of the source. (d), (e) and (f) Same as (a), (b) and (c), respectively, except with CPMLs of 10-elements width.

seismograms obtained with complete P_2 modelling (compare Figs 9a and 5a). Therefore, taking into account that the computation time and the memory consumption of the P_2/P_1 simulation are nearly half of those required with the full P_2 modelling, we can conclude that this mixed numerical scheme is of interest. It should be noticed that it is possible to adopt a weighted partitioning approach to overcome partly load balancing issues. Nevertheless, it does not prevent from using our mixed scheme approach which allows a significant reduction of the number of CPML memory variables. Actually, our strategy is totally compatible with a weighted partitioning and the combination of both would be more efficient than using only one of them. We should also stress that the saving in CPU time and memory provided with this kind of low-cost absorbing boundary condition is crucial for large 3-D simulations, and this becomes a must in the context of 3-D seismic imaging applications that require a lot of forward problems, such as FWI.

5 ACCURACY OF DG-FEM WITH TETRAHEDRAL MESHES

There are a variety of studies in the literature concerning the dispersive and dissipative properties of DG-FEM with reference to

wave-propagation problems. To cite but a few examples: Ainsworth *et al.* (2006) provided a theoretical study for the 1-D case; Basabe *et al.* (2008) analysed the effects of basis functions on 2-D periodic and regular quadrilateral meshes; and Käser *et al.* (2008) discussed the convergence of the DG-FEM combined with ADER time integration and 3-D tetrahedral meshes. More related to our particular concern here, Delcourte *et al.* (2009) provided a convergence analysis of the DG-FEM with a centred flux scheme and tetrahedral meshes for elastodynamics. They demonstrated the sensitivity of the DG-FEM to the mesh quality, and they proved that the convergence is limited by the second-order time integration we have used in this study, despite the order of the basis function.

5.1 Convergence study

We present a convergence analysis of the DG-FEM P_2, P_1 and P_0 schemes following the approach of Delcourte *et al.* (2009). The analysis is based on the propagation of an eigenmode in a unit cube with a free surface condition applied at all faces. The properties of the cube are $V_P = 1 \, \mathrm{m \, s^{-1}}$, $V_S = 0.5 \, \mathrm{m \, s^{-1}}$ and $\rho = 1 \, \mathrm{kg \, m^{-3}}$. According to these parameters, the solution of the eigenmode $(1,1,1)$
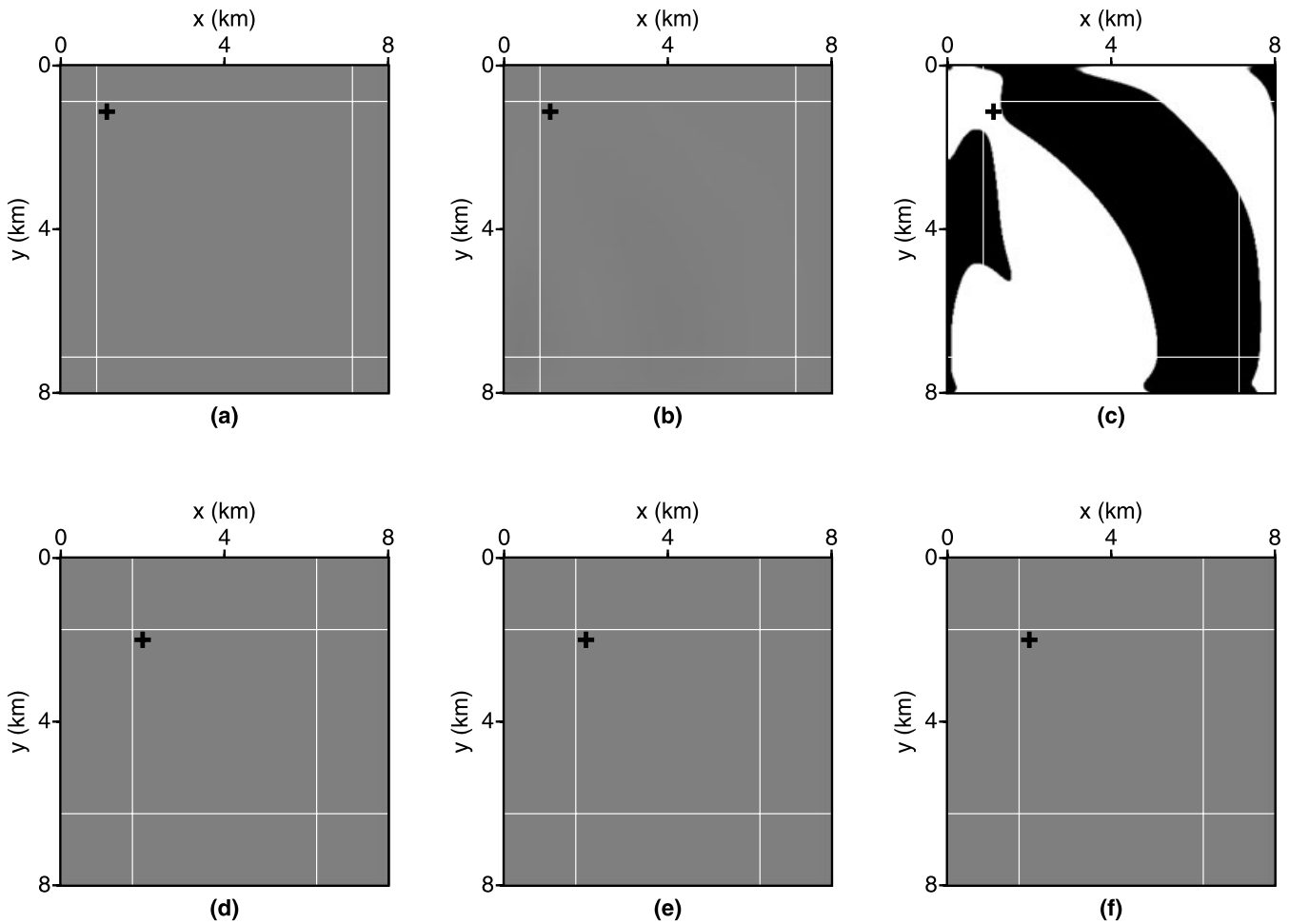
Figure 7. (a), (b) and (c) Snapshots of the velocity component v_x in the plane xy that contains the source location at 10, 20 and 30 s, respectively. The amplitude is plotted without any magnification factor. The modelling was carried out with P_2 interpolation. M-CPMLs with five-elements width and 10 per cent of the damping profile added onto the directions parallel to the layer were applied at all edges of the model. White lines, the limits of the M-CPMLs; black cross, the position of the source. (d), (e) and (f) Same as (a), (b) and (c), respectively, except with M-CPMLs of 10-elements width.

Table 1. Computation times for updating the velocity and stress wavefields in one element for one time step. These values correspond to average computation times for a computing platform with bi-processor quad core Opteron 2.3 GHz CPUs interconnected with Infiniband 20 at Gb s^{-1}.

Approximation order	Element outside CPML (μs)	Element inside CPML (μs)
P_0	2.6	3.6
P_1	5.0	8.3
P_2	21.1	29.9

is given by

$$v_x = \cos(\pi x)\left[sin(\pi y) - \sin(\pi z)\right]\cos(\Omega t)$$

$$v_y = \cos(\pi y)\left[sin(\pi z) - \sin(\pi x)\right]\cos(\Omega t)$$

$$v_z = \cos(\pi z)\left[sin(\pi x) - \sin(\pi y)\right]\cos(\Omega t)$$

$$\sigma_{xx} = -A\sin(\pi x)\left[sin(\pi y) - \sin(\pi z)\right]\sin(\Omega t)$$

$$\sigma_{yy} = -A\sin(\pi y)\left[sin(\pi z) - \sin(\pi x)\right]\sin(\Omega t)$$

$$\sigma_{zz} = -A\sin(\pi z)\left[sin(\pi x) - \sin(\pi y)\right]\sin(\Omega t)$$

$$\sigma_{xy} = \sigma_{xz} = \sigma_{yz} = 0, \tag{29}$$

where $A = 1/\sqrt{2}$ and $\Omega = \pi/\sqrt{2}$. In order to assess the convergence rate of the method, we made several tests with different unstructured tetrahedral meshes with the characteristics summarized in Table 2. The initial conditions are imposed at each node of the elements by setting the velocities at $t = 0$ and the stresses at $t = \Delta t/2$ following eq. (29). We place a bunch of receivers according to a cartesian grid that matches the size of the cube. The spacing between receivers is 0.1 m, making a total number of 1331 receivers ($11 \times 11 \times 11$). At each receiver, a sinusoidal signal with a period of $T = 2\sqrt{2}$ s should be observed. This monochromatic signal corresponds to the propagation of P-waves across the cube that are continuously reflected at the cube faces. Consequently, we can establish a relationship between the simulation time and the propagated distance. In the Fig. 10(a), we present the normalized rms error between the analytical and numerical solutions at $t = 5T$ and at $t = 50T$, corresponding to a propagation of 5 and 50 wavelengths, respectively. We can observe that no convergence is achieved with P_0 while a second-order convergence is observed for both P_1 and P_2 at $t = 5T$. As expected, an increase of the error is seen at longer times, resulting from the accumulation of errors with time iterations. At $t = 50T$, a second-order convergence is still observed for P_1 while the convergence of P_2 becomes more
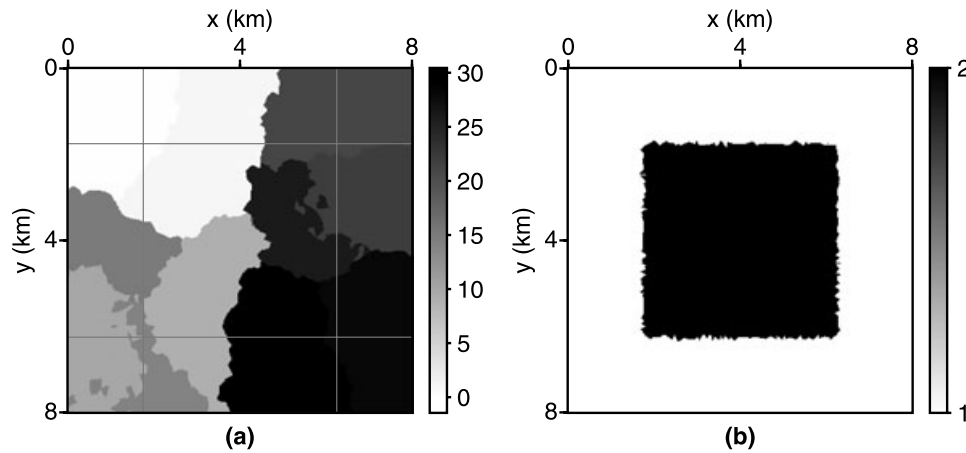
Figure 8. (a) Layout of the subdomains obtained with the partitioner METIS (Karypis & Kumar 1998) along the *xy* plane that contains the source location. Grey lines, the limits of the CPMLs. The mesh was divided into 32 partitions, although only a few of these are visible on this cross-section. (b) View of the approximation order per element along the same plane. Black, the P_2 elements; white, the P_1 elements.
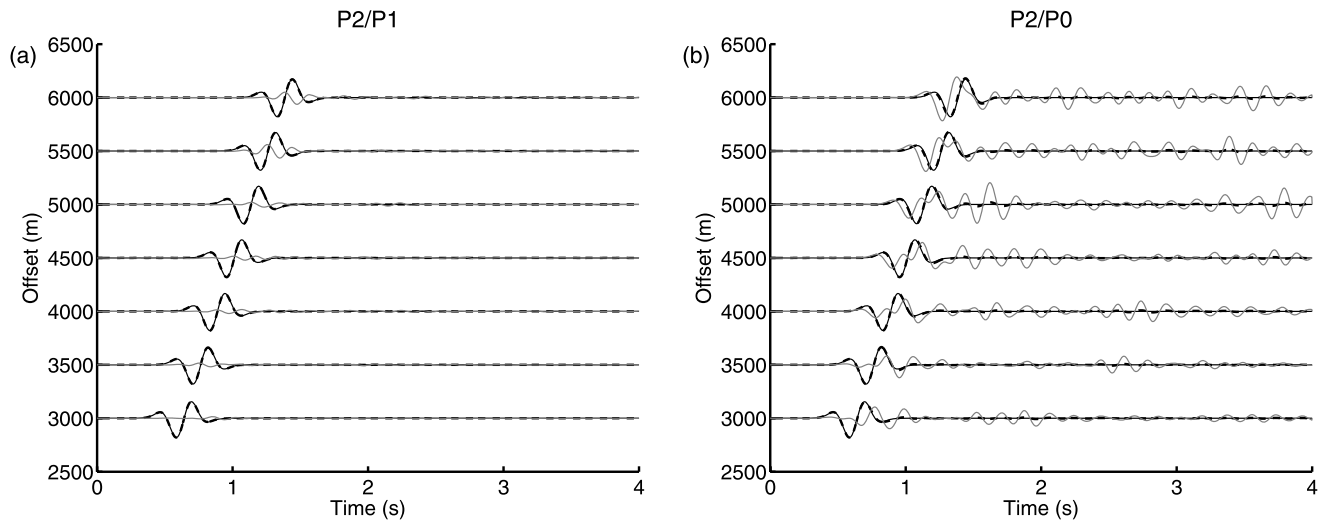

Figure 9. (a) Seismograms of the velocity component v_x. The amplitude of each seismogram is normalized. The modelling is done with P_1 in the CPMLs and P_2 inside the medium. Black continuous line, numerical solution in large model without reflection in the time window; dashed line, numerical solution with 10-elements width CPMLs; grey line, residuals magnified by a factor of 10. (b) Same as (a) except the modelling is done with P_0 in the CPMLs and P_2 inside the medium.

Table 2. Average edge length, minimum and maximum insphere radius and number of elements of the unstructured tetrahedral meshes used for the convergence study.

Mesh	1	2	3	4	5	6
Average edge (m)	0.19	0.12	0.08	0.05	0.04	0.03
Min. insphere radius (m)	0.0203	0.0132	0.0078	0.0048	0.0030	0.0019
Max. insphere radius (m)	0.0486	0.0304	0.0211	0.0155	0.0117	0.0087
Number of elements	1561	5357	17 932	49 822	154 297	388 589

erratic. The seismograms of Figs 11(a) and (a) represent the v_x component observed at short and long times, respectively. These seismograms have been recorded at the position ($x = 0$ m, $y = 0$ m, $z = 0.5$ m) with the mesh # 4. At short times, we can see a good match between the numerical and analytical solutions for both P_1 and P_2 schemes. Concerning the P_0 scheme, we can notice a strong distortion of the sinusoidal signal with a apparent period that is shorter than the analytical one. We can conclude that the P_0 scheme does not provide accurate results with unstructured tetrahedral meshes.

At long times, the agreement is still good for P_2 (thus explaining the slow convergence observed when using finer meshes) but we can observe a strong delay for the P_1 scheme. The delay is reduced when using finer meshes as indicated by the convergence curve in Fig. 10(a). In terms of precision and efficiency, the gain from the P_2 scheme compared with the P_1 scheme can be evaluated from Fig. 10(b). For the same level of precision, the computation time of the P_2 modelling is nearly two orders of magnitude lower than the computation time of the P_1 modelling.
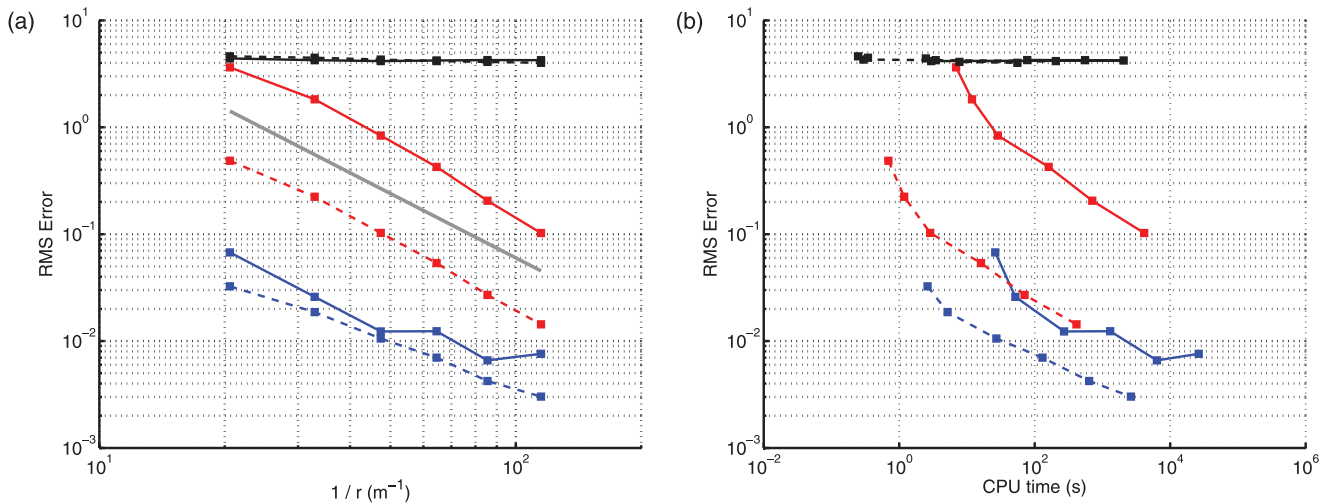
Figure 10. (a) Root mean square error between the analytical and numerical solutions versus the inverse of the maximum insphere radius r. Black dashed line, the error against the P_0 solution at $t = 5T$; black continuous line, the error against P_0 at $t = 50T$; red dashed line, the error against the P_1 solution at $t = 5T$; red continuous line, the error against P_1 at $t = 50T$; blue dashed line, the error against the P_2 solution at $t = 5T$; blue continuous line, the error against P_2 at $t = 50T$; grey curve, second-order slope. (b) Same as (a) except the root mean square error is plotted versus the elapsed computation time. The tests have been performed with 32 CPUs on a computing platform with bi-processor quad core Opteron 2.3 GHz CPUs interconnected with Infiniband at 20 Gb s^{-1}.
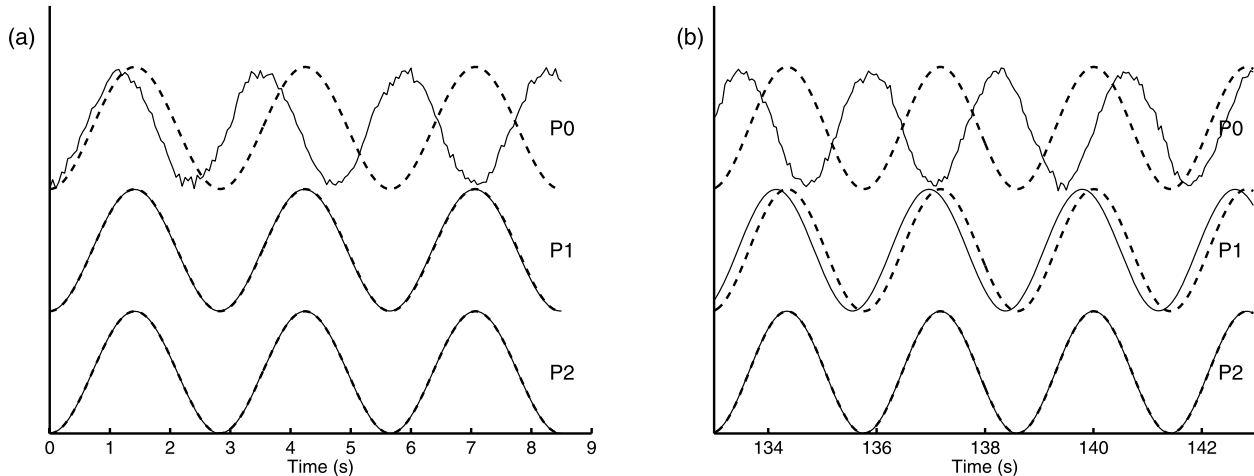

Figure 11. (a). Seismograms of velocity component v_x computed with the P_2, P_1 and P_0 schemes for $t \in [0, 3\,T]$. Continuous line, the DG-FEM solution; dashed line, the analytical solution. (b) Same as (a) for $t \in [47T, 50T]$.

5.2 Accurate modelling of surface waves

Accurate modelling of surfaces wave is crucial for seismological studies, such as for the prediction of site effects or FWI of land seismic data, where the receivers are usually located on the free surface. For simple geometries, some analytical solutions exist. The propagation of waves along the surface of an elastic half space was discussed by Lamb (1904) for a force located on the surface, and an analytical solution was defined by Garvin (1956) for the buried line-source problem. Nevertheless, in the case of complex topographies, a numerical method needs to be used. For this, a method suitable for unstructured meshes has major advantages. In the following, for validation purposes, we consider a homogeneous, isotropic and purely elastic medium with a planar free surface, and we adopt the experimental set-up defined in the WP1_HHS1 test case of the SPICE test code validation project (Moczo *et al.* 2005). The model dimensions are 20 km × 20 km × 10 km in the directions x, y and z, respectively. The physical properties are given by $V_P = 6000$ m s^{-1}, $V_S = 3464$ m s^{-1} and $\rho = 2700$ kg m^{-3}. The source is a point

dislocation with the only non-zero moment tensor component M_{xy}. The moment-rate time history is given by

$$M_{xy}(t) = M_0 \, \frac{t}{T^2} \, \exp\left(-\frac{t}{T}\right),$$

with $M_0 = 10^{18}$ Nm and $T = 0.1$ s. Considering a maximum frequency of 5 Hz, the minimum wavelength is 693 m. The source and receiver locations are given in Table 3. The distance between the source and the receivers varies from 1 to 16 $\lambda_{\min}$. We performed the computation with the mixed scheme, with P_2 elements in the medium and P_1 elements in the CPMLs. Absorbing layers were applied at all edges of the model, except at the top, where a free surface condition was used. Figs 12(a) and (b) allow a comparison of the seismograms of the components v_x and v_z, respectively, obtained with DG-FEM and with the reflectivity method (Bouchon 1981; Coutant 1989). All of these seismograms were filtered between 0.13 and 5 Hz. With an average mesh spacing of 3 elements per wavelength, a good match is seen between the analytical and numerical solutions for all of the traces. Exceptions are found for

Table 3. Source and receiver locations for the planar free-surface modelling.

Type	X (m)	Y (m)	Z (m)
Source	0	0	−693
Receiver #1	0	693	0
Receiver #2	0	5543	0
Receiver #3	0	10 932	0
Receiver #4	490	490	0
Receiver #5	3919	3919	0
Receiver #6	7348	7348	0
Receiver #7	577	384	0
Receiver #8	4612	3075	0
Receiver #9	8647	5764	0

the component v_z in traces #1, 2 and 3, where the DG-FEM fails to reproduce strictly null signals, but exhibits weak residuals. These residuals might be due to the spatial support of the source, which does not coincide with a pure Dirac in space, as depicted in Fig. 3(c).

6 *HP*-ADAPTIVITY

6.1 Two-step refinement approach

One of the most interesting aspects of the DG-FEM is the possibility to mix approximation orders without any special efforts. This feature relies on the local support of the basis functions, which are discontinuous between the elements, as was introduced in Section 2, and is referred to as *p*-adaptivity. When combined with mesh refinement, this method becomes *hp*-adaptive. As in the initial study of Babuska & Suri (1990), *hp*-adaptive FEMs associated with *a posteriori* error estimates have gained a lot of interest due to the exponential rates of convergence seen with the correct combination of *h*- and *p*- refinements. In the present study, we propose to define a simple *a priori* error estimate to predict the required approximation order for each element. Our approach is based on two major steps. The first refers to the mesh construction, with the intention to build a tetrahedral mesh that is locally adapted to the media properties. Initially, a mesh is generated that roughly satisfies the discretization required by the target approximation order. At the very beginning of the procedure, the mesh can even be regular. Afterwards, the elements are checked against the physical properties of the medium,

and the list of elements that need to be refined is used for the next iteration. The process is repeated until the list of elements to refine is empty. We used to build and refine our meshes with the tool TETGEN (Si & Gärtner 2005) which allows to specify for each element the maximum authorized volume. To compute the optimal volume for each element, we usually define a maximum ratio between the insphere radius and the wavelength and then we evaluate the corresponding volume of an equilateral tetrahedron. Given the complexity of the medium to be discretized, tetrahedral mesh generators can produce ill-shaped tetrahedra even if quality criteria are used. A common practice is to limit the aspect ratio, which is defined by the ratio between the maximum side length and the minimum height of the elements. Nevertheless, despite robust algorithms, like the Delaunay refinement algorithm of Shewchuk (1998), some almost flat elements can be present at the end of the refinement process, which are known as slivers. Besides these slivers, another critical phenomenon can occur where there are abrupt contrasts in the physical properties. In these situations, the refinement algorithm might not be able to perform the optimal discretization. This occurs when the size of the elements cannot vary as fast as the medium properties for geometrical reasons. In that case, some elements are necessarily undersized. Consequently, the construction of an ideal mesh is a difficult task, and a large range of element sizes is often seen in constrained meshes. To mitigate the negative effects of the badly sized elements, we propose to downgrade these elements with lower approximation orders. This is done in the second step of our refinement approach, which is devoted to the *p*-adaptivity.

6.2 Numerical results

Our intention here, is to illustrate the benefits of the *p*-adaptivity. For that purpose, we consider the case of the eigenmode propagation in the unit cube presented in Section 5.1 and introduce a refined area in meshes #1, 2 and 3 in order to create artificially a large range of element sizes. We obtain the new meshes #1′, 2′ and 3′ by defining a cubic zone of size 0.1 m × 0.1 m × 0.1 m in the middle of the model where the average edge length is ten times smaller than *h*, the average edge length in the surrounding mesh. The characteristics of the meshes can be found in Table 4. The ratio between the maximum and minimum insphere radius have been significantly increased compared to the uniform meshes used
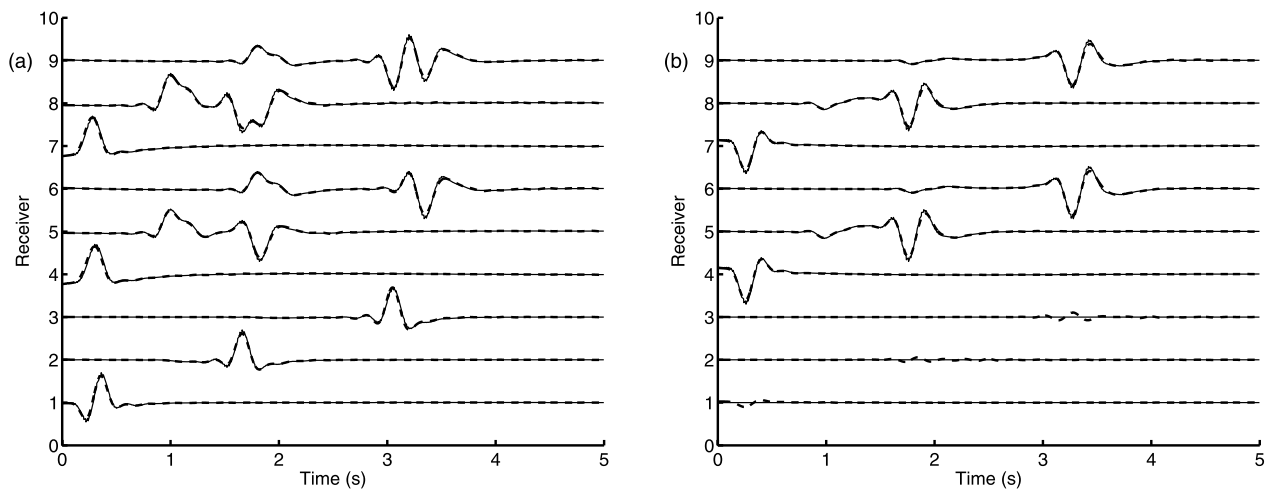

Figure 12. (a) Seismograms of the velocity component v_x computed for the planar free-surface modelling of the SPICE test code validation project. Continuous line, the analytical solution provided by the reflectivity method; dashed line, the DG-FEM solution. (b) Same as (a) with the component v_z.

Table 4. Minimum and maximum insphere radius and number of elements of the unstructured tetrahedral meshes with a refined area.

Mesh	1′	2′	3′
Min. insphere radius (m)	0.0017	0.0010	0.0007
Max. insphere radius (m)	0.0425	0.0292	0.0198
Number of elements	6952	26 374	82 668

previously (compare with Table 2). The cross section of the mesh #3′ in Fig. 13(a). allows to see the refined area in the center of the model. For the *p*-adaptivity, we adopted the following criteria: if the insphere radius is comprised between $h/30$ and $h/10$, the approximation order is downgraded to P_1, and if the radius is smaller than $h/30$, the approximation order is downgraded to P_0. This strategy is depicted in Fig. 14, where for each approximation order, the time step evaluated with eq. (15) *versus* the insphere radius of one single equilateral tetrahedron is shown. When applying these criteria, the time step does not decrease uniformly according to the size of the element. Instead, two jumps (Fig. 14, dashed line) allow the time step to increase despite the reduction in the element size. These jumps are due to the decrease in the approximation order from P_2 to P_1, and from P_1 to P_0. According to the adopted criteria, we obtain the distribution of approximation orders indicated in Table 5. The number of downgraded elements is quite important and represent for all meshes approximatively 60 per cent. Nevertheless, the downgraded elements are mostly located in the vicinity of the refined area as shown in Fig. 13(b) and represent in average only 3 per cent of the volume of the model. Moreover, despite the fact that the P_0 scheme does not provide accurate results, the introduction of such elements allows a drastic increase of the time step by a factor of five. The impact of the downgraded elements can be analysed with Fig. 15(a) showing the normalized rms error between the analytical, the P_2 and the *p*-adaptive numerical solutions at $t = 50T$. Actually, the *p*-adaptive scheme exhibits an error which is comparable to the complete P_2 modelling except for the mesh #3′, where we observe a particular behavior of the P_2 scheme with an increase of the error despite the mesh spacing has been reduced. This indicates that a large distribution of element sizes has an effect on the convergence on the P_2 scheme. On the contrary, the *p*-adaptive scheme seems
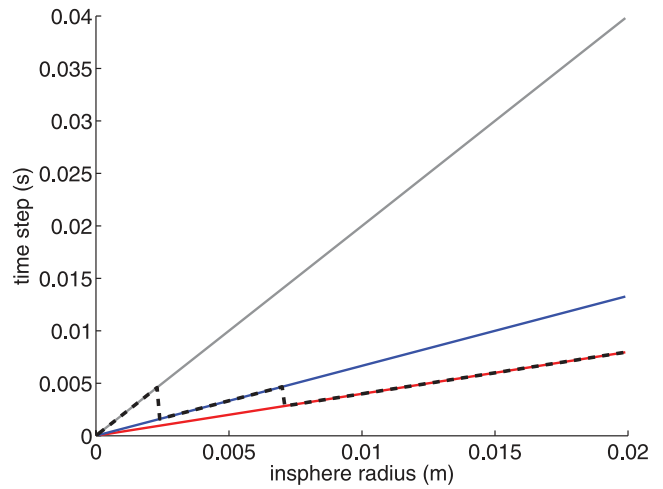

Figure 14. Time step *versus* the insphere radius of one single equilateral tetrahedron computed with eq. (15), for different approximation orders. Grey curve, P_0; blue curve, P_1; red curve, P_2; dashed line, the *p*-adaptive approach used for mesh #3′.

less sensitive and preserves the second-order convergence. From a computational point of view, the benefit of the approach appears in Fig. 15(b) where the error is represented versus the computation time. For the same computation time, the *p*-adaptive approach shows a better misfit than the full P_2 modelling, as indicated by the position of the *p*-adaptive curve at the left of the P_2 curve. The *hp*-refinement provided by DG-FEM is particularly interesting in the case of complex refined meshes where small elements are generally produced by tetrahedral mesh generators. The efficiency of our approach in such cases is illustrated in the next section.

7 APPLICATION TO COMPLEX MEDIUM

We here demonstrate the potential of DG-FEM with *hp*-adaptivity in a challenging seismological model, where the computation of the surface waves is critical for the prediction of site effects. These phenomena arise when the ground motion caused by an earthquake
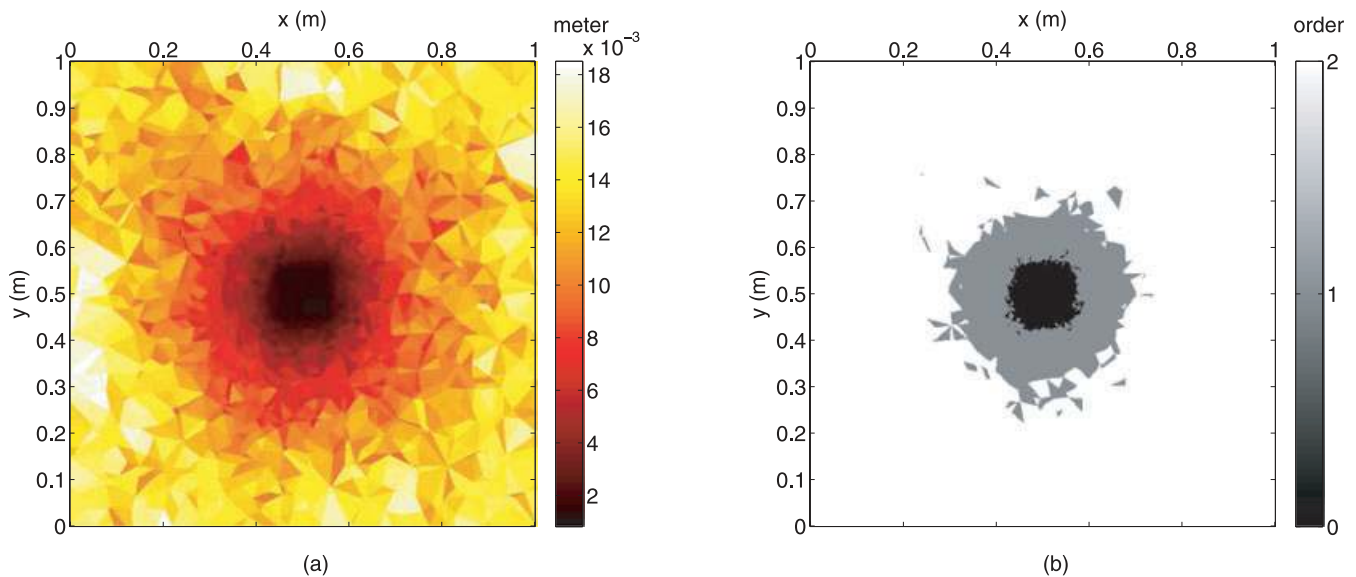

Figure 13. (a) View of the mesh in the *xy* plane at $z = 0.5$ m, showing the size of the elements (insphere radius) in the mesh #3′. (b) Same as (a) with the approximation order associated with each element. White, P_2 elements; grey, P_1 elements; black, P_0 elements.

Table 5. Number of elements per approximation orders and time steps for the complete P_2 and the *p*-adaptive modelling.

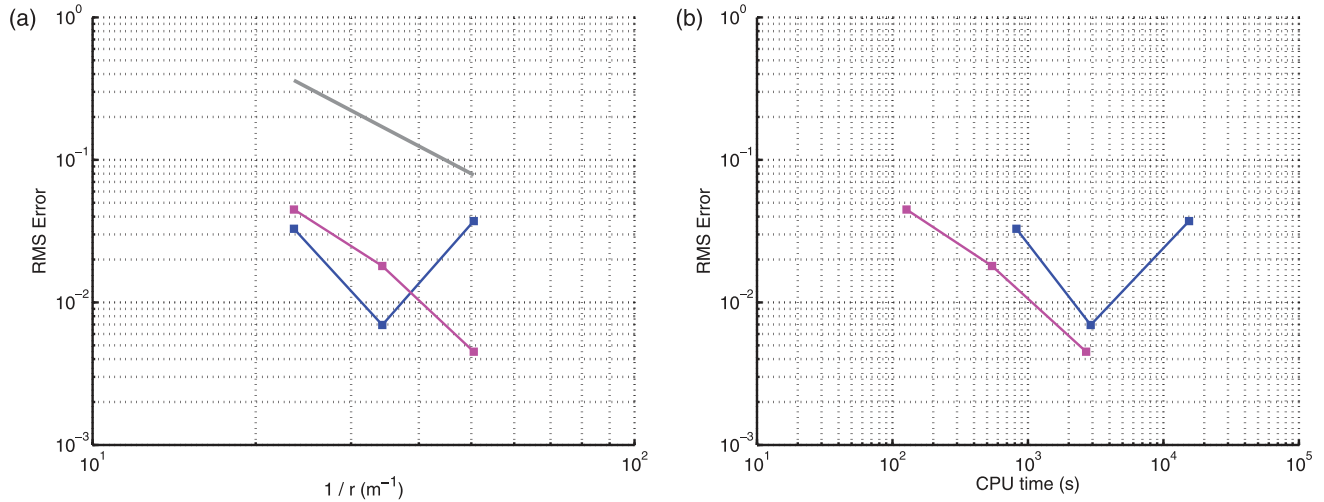|	Nb P_0 elements	Nb P_1 elements	Nb P_2 elements	Time step
Full P_2 scheme with mesh 1′	0	0	6952	0.0006745
p-adaptive scheme with mesh 1′	2520	1606	2826	0.0033372
Full P_2 scheme with mesh 2′	0	0	26 374	0.0004187
p-adaptive scheme with mesh 2′	10 883	5849	9642	0.0020934
Full P_2 scheme with mesh 3′	0	0	82 668	0.0002737
p-adaptive scheme with mesh 3′	34 176	17 483	31 009	0.0013687

Figure 15. (a) Root mean square error between the analytical and numerical solutions versus the inverse of the maximum insphere radius r at $t = 50T$. Blue line, the error against the P_2 solution; pink line, the error against the *p*-adaptive solution; grey curve, second-order slope. (b) Same as (a) except the root mean square error is plotted versus the elapsed computation time. The tests have been performed with 32 CPUs on a computing platform with bi-processor quad core Opteron 2.3 GHz CPUs interconnected with Infiniband at 20 Gb s^{-1}.

is amplified by geological structures. Site effects can be related to a sedimentary basin, like for the great earthquake in Mexico in 1985 (Campillo *et al.* 1989; Kawase 2003). The importance of site effects and their study were the main motivation for setting-up worldwide test sites. Here, we consider the EUROSEISTEST verification and validation project (Chaljub *et al.* 2009), and address the issue of modelling the ground motion in a basin structure. We compare the results obtained with our method against results computed with SEM.

7.1 Description of EUROSEISTEST verification and validation project

The EUROSEISTEST verification and validation project refers to the geological structure of the Mygdonian sedimentary basin about 30 km E–NE of the city of Thessaloniki (northern Greece). It mainly consists of a sedimentary basin with extreme low velocities and a high Poisson ratio, embedded in high velocity bedrock. The velocity structure of the area is well known along the central section *AB* (Fig. 16b), following a large number of geophysical and geotechnical measurements (Jongmans *et al.* 1998), surface and borehole seismic prospecting, and electrical soundings and microtremor recordings. The 3-D structure in the whole graben was then extrapolated from this central profile, taking into account information from many single-point microtremor measurements, some array microtremor recordings, one EW refraction profile, and old deep boreholes drilled for water-exploration purposes (Raptakis *et al.* 2005; Manakou *et al.* 2007). The sediment thickness indeed increases both to the West and the East of the central profile, which

corresponds to a buried pass between two thicker subbasins. For the verification part of the EUROSEISTEST project, a smooth vertical gradient without any lateral variation was considered. Inside the basin, the velocities vary with the depth as follows

$$V_P = 1000 + 100\sqrt{d}$$
$$V_S = 200 + 32\sqrt{d},$$

where V_P and V_S are expressed in m s^{-1}, and d is the depth in m. Table 6 summarizes the properties of the EUROSEISTEST model. The ratio between the maximum and minimum *S*-wave velocities is 17.2. This high factor favours the use of unstructured meshes, as a large range of different element sizes is expected. Indeed, small elements are required in the basin area while larger ones can be used in the bedrock. The size of the model is 16 km × 15 km × 8 km in the directions *x*, *y* and *z*, respectively. M-CPMLs of 2 km width are applied at all edges of the model, except at the top, where a free surface condition is used. The model topography is flat. Figs 16(a) and (b) show the *P*- and *S*-wave velocities, respectively, on the free surface in the *xy* plane. In these figures, the complex shape of the basin and the abrupt contrast of velocity at the basin border can be seen. The source is located 5 km below the basin, and it acts as a double-couple mechanism that represents a small earthquake with a corner frequency of 4 Hz (Fig. 17). The epicentre is indicated with a yellow star in Fig. 16(a). The minimum propagated wavelength is 50 m, and the largest dimension of the model is 320 λ. We considered seven receivers, as marked with numbered green triangles in Fig. 16(a), at strategic positions of the true EUROSEISTEST array. All of these receivers lie on the free surface, except receiver #7,
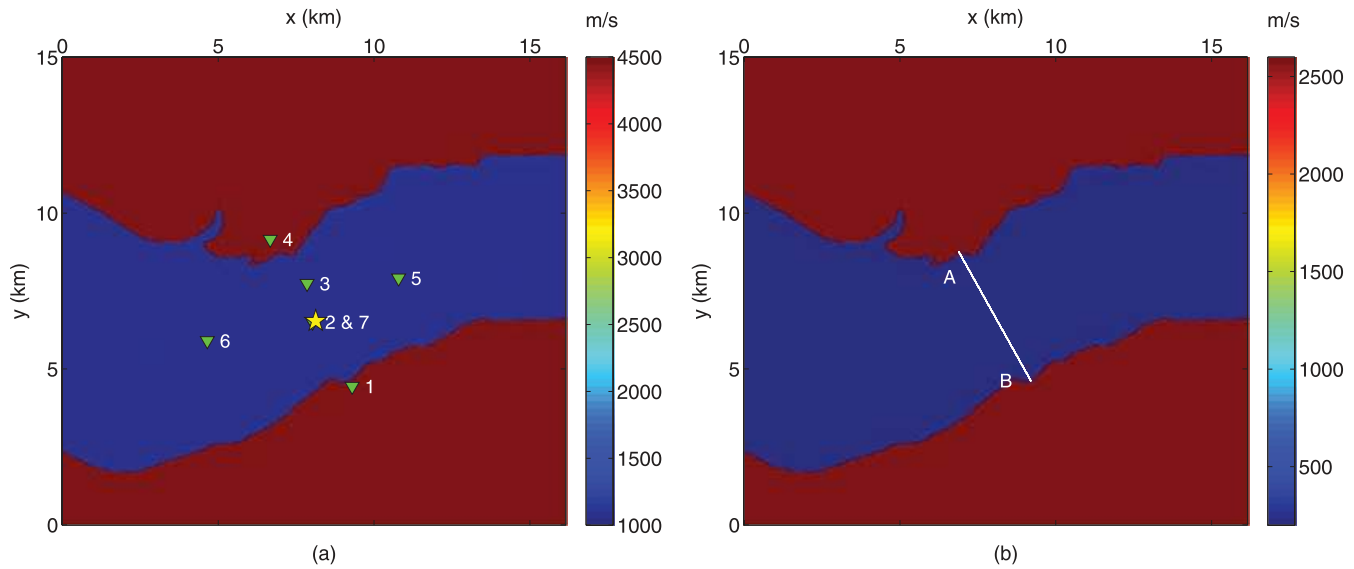
Figure 16. (a) View of the mesh in the *xy* plane at *z* = 0 m, showing the *P*-wave velocity associated with each element in the EUROSEISTEST model. Numbered green triangles, the receivers; yellow star, source epicentre. (b) Same with the *S*-wave velocity associated with each element. The position of the cross-section *AB* is indicated by the white line.

Table 6. The properties of the geological structures of the EUROSEISTEST model.

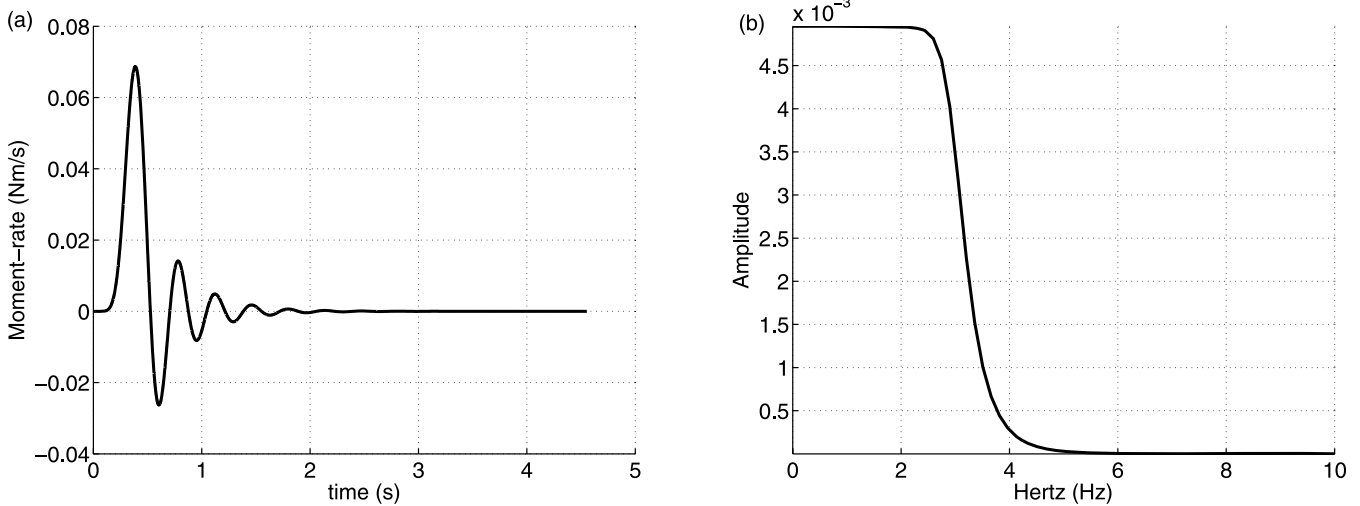|	*P*-wave velocity (m s^{-1})	*S*-wave velocity (m s^{-1})	Density	Ratio V_P / V_S	Max. depth
Basin	1000–3027	200–848	2100 kg m^{-3}	5.00–3.57	411 m
Bedrock	4500–6144	2600–3444	2600–2755 kg m^{-3}	1.73–1.78	8 km

Figure 17. (a) Moment-rate function of the source used for the EUROSEISTEST modelling. (b) Amplitude spectrum of the source.

which is buried at 197 m depth just above the source. Receivers #1 and #4 are located on the bedrock, and the others are located within the basin area.

7.2 Numerical results

For the SEM calculations, the size of the computational domain was 16.14 km × 29.31 km × 7.86 km, and local absorbing boundary conditions were imposed at the lateral and bottom boundaries, following Komatitsch & Vilotte (1998). The mesh is based on a conforming layer-cake topology (Komatitsch *et al.* 2004) where the elements are deformed to follow the sediment-bedrock interface,

except for depths shallower than a threshold value, which was set to 80 m for the basin. For the elements close to the valley edges, the sediment-bedrock discontinuity is approximated by assigning different material values to the collocation points inside the elements. Note that because of the large *P*-wave velocity in the shallow bedrock, the choice of the threshold depth directly controls the time step authorized by the CFL stability condition, and therefore the total CPU time of the simulation. For the DG-FEM calculations, the size of the numerical model was 20.14 km × 19 km × 8 km in the directions *x, y* and *z*, respectively, including M-CPMLs of 2 km width at all edges of the model, except at the top, where a free-surface condition was used. We adopted the two-step refinement
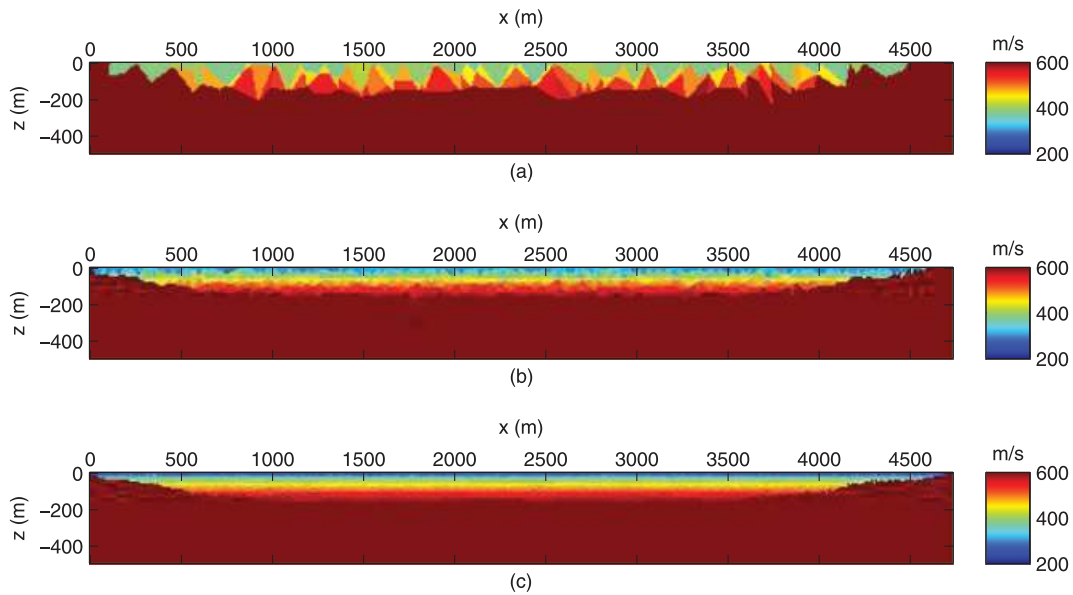
Figure 18. (a) Cross-section *AB* of the mesh at the first iteration of the *h*-refinement showing the *S*-wave velocity associated with each element in the EUROSEISTEST model. (b) Same as (a) at the second iteration of the *h*-refinement. (c) Same as (a) at the sixth and last iteration of the *h*-refinement.
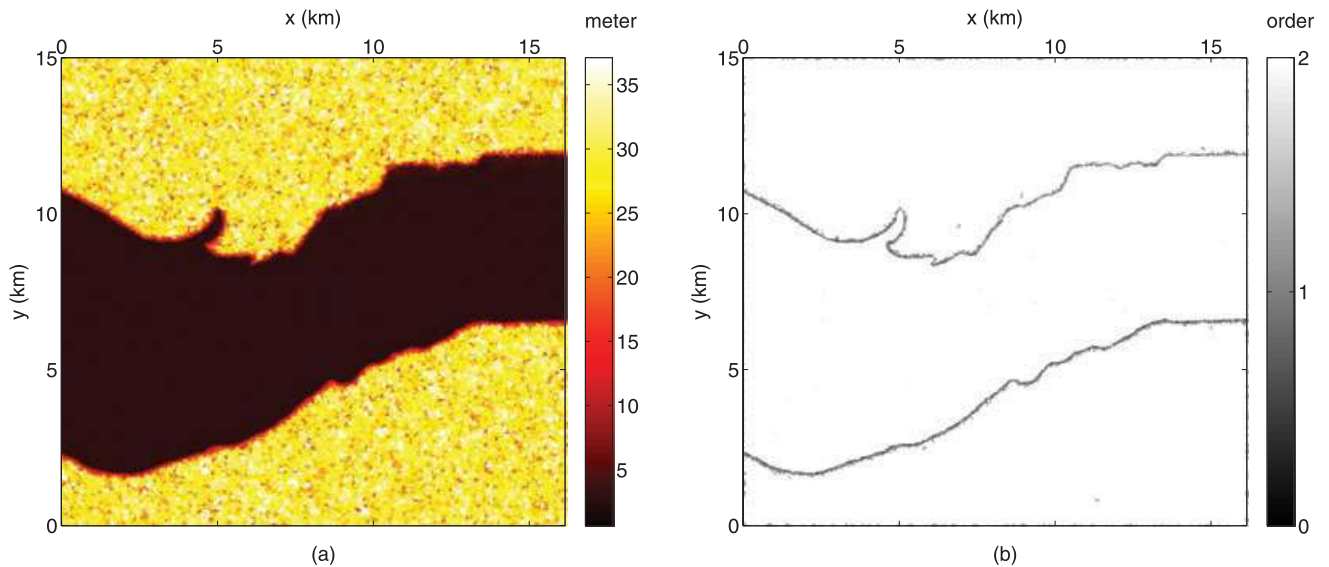

Figure 19. (a) View of the mesh in the *xy* plane at $z = 0$ m, showing the size of the elements (insphere radius) in the EUROSEISTEST model. (b) Same as (a) with the approximation order associated with each element. White, P_2 elements; grey, P_1 elements; black, P_0 elements.

approach explained in the previous section. In the first step, we built an *ad hoc* tetrahedral mesh with TETGEN. A total of six mesh refinement iterations were required to reach an adaptive discretization of three elements per λ_S. Figs 18(a), (b) and (c) show the distribution of the *S*-wave velocity in the cross-section *AB* for the first, second and last iterations of the *h*-refinement process, respectively. Due to the extremely low velocities in the basin, the automatic refinement process produced very small elements, which resulted in a fine and regular discretization of the basin shape. Fig. 19(a) shows the size of the elements (insphere radius) on the free surface. As expected, smaller elements are found in the basin area rather than in the bedrock. In this example, we have taken advantage of the tetrahedral mesh refinement. Indeed, the volume of the basin represents 0.8 per cent of the complete volume of the model and it contains 72 per cent of the total number of mesh elements. In the second step, we made

use of *p*-adaptivity to reduce the number of time steps. We adopted the following criteria: if the insphere radius is between $\lambda_S/120$ and $\lambda_S/40$, the approximation order is downgraded to P_1, and if the insphere radius is smaller than $\lambda_S/120$, the approximation is downgraded to P_0. While most of the tetrahedral elements are adequate for P_2, the badly sized elements are computed with lower approximation orders. We end up with a mesh that contains in total 16.3 million elements and 131.0 million DOF. The approximation orders are distributed as follows: 67.04 per cent P_2 elements, 32.67 per cent P_1 elements (with 28.66 per cent elements in the M-CPMLs), and 0.29 per cent P_0 elements. This strategy is shown in Fig. 19(b), where the approximation order is shown for each element located on the free surface. Almost all of the elements are P_2 elements, except for those with inappropriate sizes, which are downgraded to P_1 or to P_0 in the worst cases. Indeed, the contact
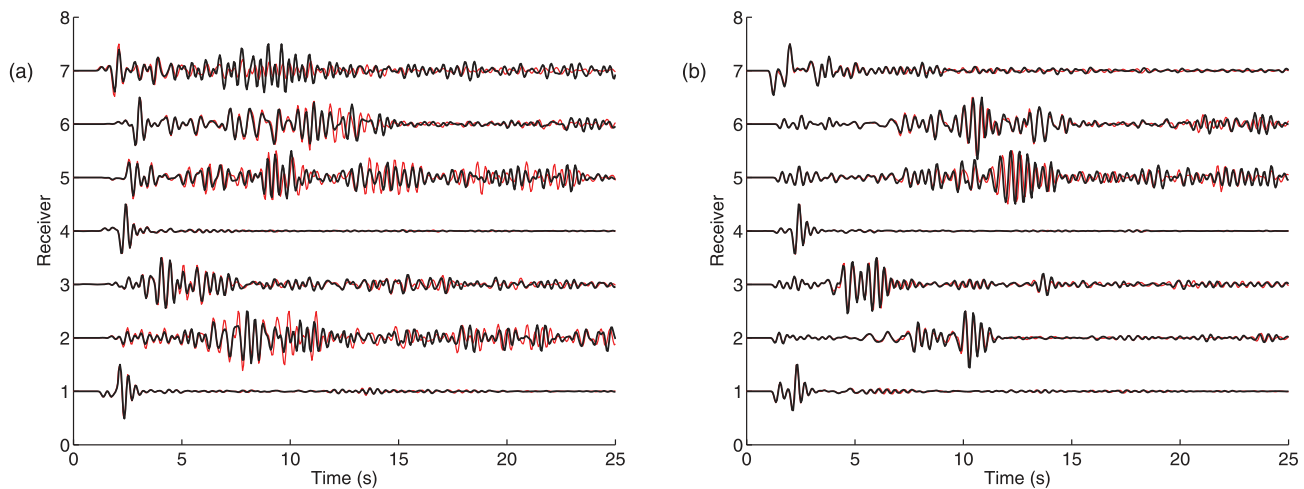
Figure 20. (a) Seismograms of the component v_x computed in the EUROSEISTEST model. Black line, with DG-FEM; red line, with SEM. (b) Same as (a) with the component v_z.

Table 7. Mesh statistics, computation time and memory allocation relative to the EUROSEISTEST modelling. the DG-FEM and SEM computations were both performed with 18 bi-xeon Quadcore CPU IBM E5420 at 2.5 GHz (making a total of 144 cores).

Method	Order	Min. edge (m)	Max. edge (m)	Nb elem.	Nb DOF	Nb steps	Nb CPUs	Elapse time (hr)	Memory (GB)
DG-FEM	$P_2/P_1/P_0$	2.5	399.8	16.3×10^6	131.0×10^6	122 565	144	52	~26
SEM	P_4	20.0	906.0	1.4×10^6	91.7×10^6	75 000	144	7	~25

between the basin and the bedrock produces a high velocity contrast that is not ideally accommodated by the tetrahedra. Therefore, some elements located in the bedrock have smaller sizes than expected, and thus can be treated with lower approximation orders. These latter are particularly visible in Fig. 19(b). Some P_1 elements also appear at the border in Fig. 19(b) where the M-CPMLs start.

The seismograms of the components v_x and v_z computed with DG-FEM and with SEM are shown in Figs 20(a) and (b), respectively. The fit between the DG-FEM and SEM solutions is almost perfect for the vertical component v_z, whatever the position of the receivers, and even at long times. On the other hand, for the horizontal component v_x, good agreement is seen for short times, of up to 6–7 s. At later times, some amplitude misfits are seen. Nevertheless, for all of the traces, the overall fit of the waveforms between the two solutions is remarkable, which indicates that the same and complex wave propagation phenomena are represented. Contrary to the SEM, for the DG-FEM, constant physical properties per element were assumed, given by the average of the properties at the four vertices of the elements. Therefore, the amplitude misfits seen in the DG-FEM seismograms might be the consequence of the approximations used in the model discretization, rather than the accuracy of the numerical method itself. The statistics related to the DG-FEM and SEM modelling are given in Table 7. Compared to DG-FEM, the number of DOF used in the SEM modelling is 30 per cent lower, and the number of time steps is nearly two-fold lower. Both of the simulations were performed on the same computing platform with 18 bi-xeon Quadcore CPU IBM E5420 at 2.5 GHz (giving a total of 144 cores). The methods required similar amounts of memory, and to obtain 30 s of wave propagation, the computation time was 7 hr with SEM and 52 hr with DG-FEM. The computation time per DOF and per step is on average 1.67 µs for DG-FEM, and 0.52 µs for SEM. Taking into account that the number of unknowns per DOF is nine with DG-FEM (with first-order velocity–stress formulation) and three with SEM (with second-order velocity formulation), these two methods yield comparable computation times

per unknown. Therefore, the relative cost of the methods depends mainly on the mesh characteristics. However, a detailed analysis is required and goes beyond the scope of this study. We can expect, that in more complicated cases (like a set of thin geological layers), the DG-FEM would be more efficient, due to the flexibility of tetrahedral meshes. In the following, we present another comparison tool that allows for a study of the misfits on the complete free surface of the model. An objective in earthquake engineering is to predict the ground motion for a realistic scenario. The map of peak ground velocity (PGV) provides a convenient representation that shows the maximum value of the norm of the velocity vector for each position on the free surface. PGV maps computed with 30 s of seismic signals are shown in Fig. 21. The fit between the PGV map computed with DG-FEM and the PGV map computed with SEM is almost perfect. On these maps, the paths followed by energetic bundles of surface waves can be seen. When they reach the basin borders, these bundles are reflected and diffracted. This behaviour can be be seen in the PGV map in the southeast part of the basin.

8 PERSPECTIVES AND CONCLUSIONS

We have proposed a DG-FEM with CPML absorbing boundary condition that benefits most from *hp*-adaptivity combined with tetrahedral meshes. The gain obtained with this method in the context of 3-D seismic elastic modelling is important when complex geological structures are considered, especially if the medium has highly contrasting physical properties. In our approach, we favour the use of low approximation orders which allows fine discretization of the medium with piecewise constant properties per element. From this point of view, an optimal compromise between precision, computational cost and adequate discretization is achieved with the P_2 interpolation. For efficient reduction of the computation time, CPMLs were designed with lower approximation orders and they allowed a saving of between 40 and 60 per cent of CPU time on large
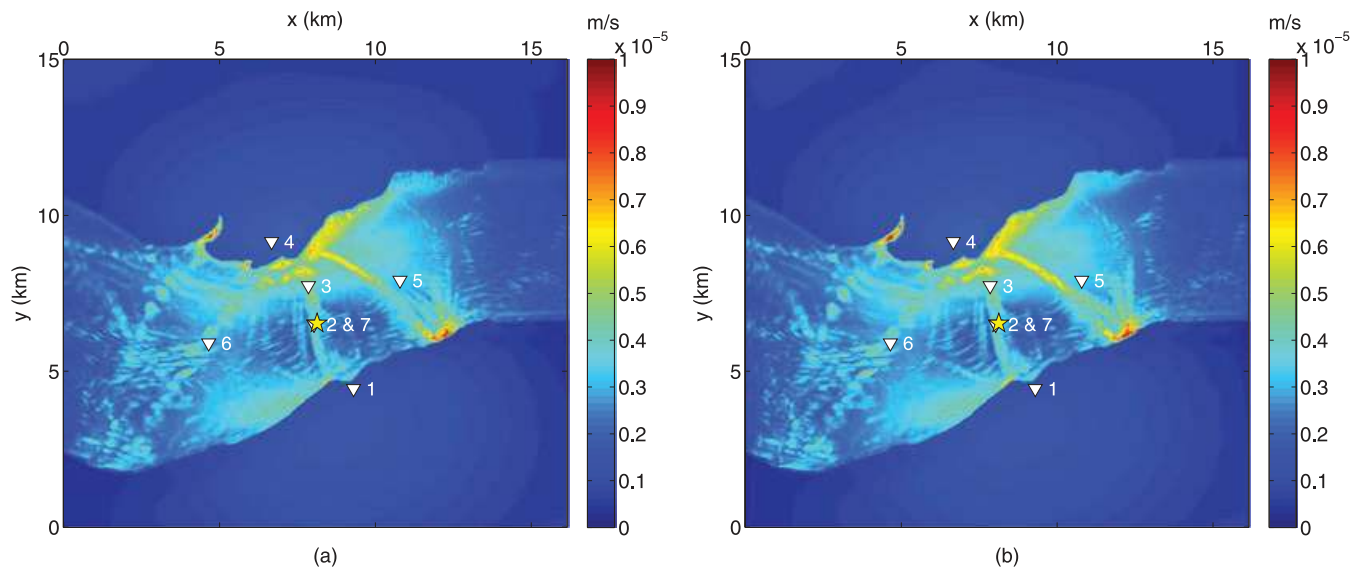
Figure 21. (a) Peak ground velocity map computed for the EUROSEISTEST modelling with DG-FEM. Numbered white triangles, the receivers; yellow star, the source epicentre. (b) Same as (a) computed with SEM.

clusters. Moreover, we mitigated the effects of ill-sized tetrahedral elements by automatically choosing the appropriate approximation order for each element, and hence we have kept the number of time steps as low as possible. In our case, the so-called *p*-adaptivity technique can reduce the number of time steps by a factor of five. Consequently, when combined with the low-cost CPMLs, computation times are generally reduced by nearly one order of magnitude, compared with the times observed with standard DG-FEM modelling using a unique approximation order. The potential and the perspectives concerning this method are numerous. For the limitations of our formulation, we note the possibility of attributing varying physical properties inside the elements. This would release the discretization constraint and would allow the use of higher approximation orders, thus reducing the number of elements and the computational cost of the simulations. For completeness, we note another possible means of releasing the discretization constraint, with non-conforming meshing, although the expected gain does not appear as crucial in the case of tetrahedral meshes as it is with hexahedral meshes. Apart from these possible evolutions, we intend to include viscoelastic rheologies (Käser *et al.* 2007) and to apply the method to realistic problems requiring appropriate discretizations of geological structures and/or large material contrasts. Due to the discontinuous nature of the method, rupture mechanisms, like earthquake dynamic rupture, might be modelled (BenJemaa *et al.* 2007, 2009; de la Puente *et al.* 2009). This method can also be applied to seismic modelling in cases of complex topographies, or be used as a forward modelling tool for FWI techniques (Tarantola 1987; Pratt *et al.* 1998).

ACKNOWLEDGMENTS

REFERENCES

Aagaard, B.T., Hall, J.F. & Heaton, T.H., 2001. Characterization of near-source ground motion with earthquake simulations, *Earthq. Spectra.,* **17,** 177–207.

Abarbanel, S., Gottlieb, D. & Hesthaven, J.S., 2002. Long-time behavior of the perfectly matched layer equations in computational electromagnetics, *J. Scient. Comput.,* **17,** 405–422.

Ainsworth, M., Monk, P. & Muniz, W., 2006. Dispersive and dissipative properties of discontinuous Galerkin finite element methods for the second-order wave equation, *J. Scient. Comput.,* **27**(1–3), 5–40.

Akcelik, V. *et al.,* 2003. High resolution forward and inverse earthquake modeling on terascale computers, in *SC'03: Proceedings of the 2003 ACM/IEEE Conference on Supercomputing,* IEEE Computer Society, Washington, DC, USA, p. 52.

Aoi, S. & Fujiwara, H., 1999. 3D finite-difference method using discontinuous grids, *Bull. seism. Soc. Am.,* **89,** 918–930.

Aoyama, Y. & Nakano, J., 1999, *RS/6000 SP: Practical MPI Programming,* IBM Corporation, Red Book edition, Texas.

Babuska, I. & Suri, M., 1990. The p and the hp versions of the finite element method: an overview, *Comp. Meth. Appl. Mech. Engng.,* **80**(1–3), 5–26.

Basabe, J.D., Sen, M. & Wheeler, M., 2008. The interior penalty discontinuous galerkin method for elastic wave propagation: grid dispersion, *Geophys. J. Int.,* **175,** 83–93.

Bécache, E., Petropoulos, P.G. & Gedney, S.G., 2004. On the long-time behavior of unsplit perfectly matched layers, *IEEE Trans. Anten. Propagat.,* **52,** 1335–1342.

BenJemaa, M., Glinsky-Olivier, N., Cruz-Atienza, V.M. & Virieux, J., 2009. 3D Dynamic rupture simulations by a finite volume method, *Geophys. J. Int.,* **178,** 541–560.

BenJemaa, M., Glinsky-Olivier, N., Cruz-Atienza, V.M., Virieux, J. & Piperno, S., 2007. Dynamic non-planar crack rupture by a finite volume method, *Geophys. J. Int.,* **171,** 271–285.

Berenger, J.-P., 1994. A perfectly matched layer for absorption of electromagnetic waves, *J. Computat. Phys.,* **114,** 185–200.

Bohlen, T. & Saenger, E.H., 2006. Accuracy of heterogeneous staggered-grid finite-difference modeling of Rayleigh waves, *Geophysics,* **71,** 109–115.

Bouchon, M., 1981. A simple method to calculate green's functions for elastic layered media, *Bull. seism. Soc. Am.,* **71**(4), 959–971.

Brossier, R., Virieux, J. & Operto, S., 2008. Parsimonious finite-volume frequency-domain method for 2-D P-SV-wave modelling, *Geophys. J. Int.,* **175**(2), 541–559.

Campillo, M., Gariel, J., Aki, K. & Sanchez-Sesma, F., 1989. Destructive strong ground motion in Mexico city: source, path, and site effects during great 1985 Michoacan earthquake, *BSSA,* **79**(6):1718–1735.

Chaljub, E. *et al.*, 2009. Assessing the capability of numerical methods to predict earthquake ground motion: the Euroseistest verification and validation project, *EOS, Trans. Am. geophys. Un.,* Abstract S43A-1968.

Chaljub, E., Capdeville, Y. & Vilotte, J.-P., 2003. Solving elastodynamics in a fluid-solid heterogeneous sphere: a parallel spectral element approximation on non-conforming grids, *J. Computat. Phys.,* **187,** 457–491.

Chaljub, E., Komatitsch, D., Vilotte, J.-P., Capdeville, Y., Valette, B. & Festa, G., 2007. *Adv. Geophysics,* **48,** 365–419.

Chew, W.C. & Liu, Q.H., 1996. Perfectly matched layers for elastodynamics: a new absorbing boundary condition, *J. Comput. Acous.,* **4,** 341–359.

Chin-Joe-Kong, M.J.S., Mulder, W.A. & Van Veldhuizen, M., 1999. Higher-order triangular and tetrahedral finite elements with mass lumping for solving the wave equation, *J. Eng. Math.,* **35,** 405–426.

Cockburn, B., Li, F. & Shu, C.W., 2004. Locally divergence-free discontinuous Galerkin methods for the Maxwell equations, *J. Computat. Phys.,* **194,** 588–610.

Collino, F. & Tsogka, C., 2001. Application of the perfectly matched absorbing layer model to the linear elastodynamic problem in anisotropic heterogeneous media, *Geophysics,* **66,** 294–307.

Coutant, O., 1989. Program of Numerical Simulation AXITRA, Research report, LGIT, Grenoble.

de la Puente, J., Ampuero, J.-P. & Käser, M., 2009. Dynamic rupture modeling on unstructured meshes using a discontinuous Galerkin method, *J. geophys. Res.,* **114,** B10302, doi:10.1029/2008JB006271.

Delcourte, S., Fezoui, L. & Glinsky-Olivier, N., 2009. A high-order discontinuous Galerkin method for the seismic wave propagation, *ESAIM: Proc.,* **27,** 70–89.

Drossaert, F.H. & Giannopoulos, A., 2007. A nonsplit complex frequency-shifted PML based on recursive integration for FDTD modeling of elastic waves, *Geophysics,* **72**(2), T9–T17.

Dumbser, M. & Käser, M., 2006. An arbitrary high order discontinuous Galerkin method for elastic waves on unstructured meshes II: the three-dimensional isotropic case, *Geophys. J. Int.,* **167**(1), 319–336.

Dumbser, M., Käser, M. & Toro, E., 2007. An arbitrary high order discontinuous Galerkin method for elastic waves on unstructured meshes V: local time stepping and p-adaptivity, *Geophys. J. Int.,* **171**(2), 695–717.

Dunavant, D.A., 1985. High degree efficient symmetrical gaussian quadrature rules for the triangle, *Int. J. Numer. Methods Eng.,* **21,** 1129–1148.

Frey, P. & George, P., 2008, *Mesh Generation.* ISTE Ltd, London & John Wiley Sons Inc, Hoboken, NJ.

Galis, M., Moczo, P. & Kristek, J., 2008. A 3-D hybrid finite-difference - finite-element viscoelastic modelling of seismic wave motion, *Geophys. J. Int.,* **175,** 153–184.

Garvin, W.W., 1956. Exact transient solution of the buried line source problem, *Proc. Roy. Soc. Lond.,* **234,** 528–541.

Graves, R., 1996. Simulating seismic wave propagation in 3D elastic media using staggered-grid finite differences, *Bull. seism. Soc. Am.,* **86,** 1091–1106.

Hesthaven, J.S. & Warburton, T., 2008, *Nodal Discontinuous Galerkin Method. Algorithms, Analysis, and Application,* Springer, New York.

Ichimura, T., Hori, M. & Kuwamoto, H., 2007. Earthquake motion simulation with multi-scale finite element analysis on hybrid grid, *Bull. seism. Soc. Am.,* **97**(4), 1133–1143.

Jacobs, G. & Hesthaven, J.S., 2006. High-order nodal discontinuous Galerkin particle-in-cell methods on unstructured grids, *J. Comput. Phys.,* **214,** 96–121.

Jongmans, D., Pitilakis, K., Demanet, D., Raptakis, D., Riepl, J., Horrent, C., Lontzetidis, K. & Bard, P.Y., 1998. Determination of the geological structure of the Volvi basin and validation of the basin response, *Bull. seism. Soc. Am.,* **88**(2), 473–487.

Karypis, G. & Kumar, V., 1998, METIS—a software package for partitioning unstructured graphs, partitioning meshes and computing fill-reducing orderings of sparse matrices, Version 4.0, University of Minnesota.

Käser, M. & Dumbser, M., 2008. A highly accurate discontinuous Galerkin method for complex interfaces between solids and moving fluids, *Geophysics,* **73**(3), 23–35.

Käser, M., Dumbser, M., de la Puente, J. & Igel, H., 2007. An arbitrary high order discontinuous Galerkin method for elastic waves on unstructured meshes III: viscoelastic attenuation, *Geophys. J. Int.,* **168**(1), 224–242.

Käser, M., Hermann, V. & de la Puente, J., 2008. Quantitative accuracy analysis of the discontinuous Galerkin method for seismic wave propagation, *Geophys. J. Int.,* **173**(2), 990–999.

Kawase, H., 2003, Site effects on strong ground motions, in *International Handbook of Earthquake and Engineering Seismology, Part B,* eds Lee, W.H.K. and Kanamori, H., Academic Press, London.

Keast, P., 1986. Moderate-degree tetrahedral quadrature formulae, *Comput. Methods Appl. Mech. Eng.,* **55,** 339–348.

Komatitsch, D. & Martin, R., 2007. An unsplit convolutional perfectly matched layer improved at grazing incidence for the seismic wave equation, *Geophysics,* **72**(5), SM155–SM167.

Komatitsch, D. & Vilotte, J.P., 1998. The spectral element method: an efficient tool to simulate the seismic response of 2D and 3D geological structures, *Bull. seism. Soc. Am.,* **88,** 368–392.

Komatitsch, D., Liu, Q., Tromp, J., Suss, P., Stidham, C. & Shaw, J.H., 2004. Simulations of ground motion in the Los Angeles basin based upon the spectral-element method, *Bull. seism. Soc. Am.,* **94,** 187–206.

Komatitsch, D., Labarta, J. & Michéa, D., 2008. A simulation of seismic wave propagation at high resolution in the inner core of the Earth on 2166 processors of MareNostrum, *Lecture Notes Comput. Sci.,* **5336,** 364–377.

Kuzuoglu, M. & Mittra, R., 1996. Frequency dependence of the constitutive parameters of causal perfectly matched anisotropic absorbers, *IEEE Microwave Guided Wave Lett.,* **6,** 447–449.

Lamb, H., 1904. On the propagation of tremors over the surface of an elastic solid, *Phil. Trans. R. Soc. Lond. Ser.,* **A 203,** 1–42.

Manakou, M., Raptakis, D., Apostolidis, P., Chavez-Garcia, F.J. & Pitilakis, K., 2007. The 3D geological structure of the Mygdonian basin (Greece), in *proceedings of the 4th International Conference on Earthquake Geotechnical Engineering,* Ref. 1686, ICEGE, Thessaloniki.

Marfurt, K., 1984. Accuracy of finite-difference and finite-elements modeling of the scalar and elastic wave equation, *Geophysics,* **49,** 533–549.

Mercerat, E.D., Vilotte, J.P. & Sanchez-Sesma, F.J., 2006. Triangular spectral element simulation of two-dimensional elastic wave propagation using unstructured triangular grids, *Geophys. J. Int.,* **166,** 679–698.

Meza-Fajardo, K. & Papageorgiou, A., 2008. A nonconvolutional, split-field, perfectly matched layer for wave propagation in isotropic and anisotropic elastic media: stability analysis, *Bull. seism. Soc. Am.,* **98**(4), 1811–1836.

Moczo, P., Ampuero, J.P., Kristek, J., Galis, M., Day, S.M. & Igel, H., 2005. The European Network SPICE Code Validation, *EOS, Trans. Am. geophys. Un.*, Abstract S13A-0180.

Moczo, P., Kristek, J., Galis, M., Pazak, P. & Balazovjech, M., 2007. The finite-difference and finite-element modeling of seismic wave propagation and earthquake motion, *Acta Physica Slovaca,* **52**(2), 177–406.

Pasquetti, R. & Rapetti, F., 2006. Spectral element methods on unstructured meshes: comparisons and recent advances, *J. Scient. Comput.,* **27,** 377–387.

Pitarka, A., 1999. 3D elastic finite-difference modeling of seismic motion using staggered grids with nonuniform spacing, *Bull. Seism. Soc. Am.,* **89**(1), 54–68.

Pratt, R.G., Shin, C. & Hicks, G.J., 1998. Gauss-Newton and full Newton methods in frequency-space seismic waveform inversion, *Geophys. J. Int.,* **133,** 341–362.

Raptakis, D.G., Manakou, M.V., Chavez-Garcia, F.J., Makra, K.A. & Pitilaks, K.D., 2005. 3D configuration of Mygdonian basin and preliminary estimate of its site response, *Soil Dyn. Earthq. Eng.,* **25,** 871–887.

Reed, W. & Hill, T., 1973. Triangular mesh methods for the neuron transport equation. Technical Report LA-UR-73-479, Los Alamos Scientific Laboratory.

Remaki, M., 2000. A new finite volume scheme for solving Maxwell's system, *COMPEL,* **19**(3), 913–931.

Roden, J.A. & Gedney, S.D., 2000. Convolution PML (CPML): an efficient FDTD implementation of the CFS-PML for arbitrary media, *Microwave Opt. Technol. Lett.,* **27**(5), 334–339.

Seriani, G. & Priolo, E., 1994. Spectral element method for acoustic wave simulation in heterogeneous media, *Finite Elements Anal. Des.,* **16,** 337–348.

Shewchuk, J.R., 1998. Tetrahedral mesh generation by delaunay refinement,

in *Proceedings of the 14th Annual Symposium on Computational Geometry,* pp. 86–95, SCG, Minneapolis, MN.

Si, H. & Gärtner, K., 2005. Meshing piecewise linear complexes by constrained delaunay tetrahedralizations, in *Proceedings of the 14th International Meshing Roundtable,* pp. 147–163, IMR, San Diego, CA.

Sirgue, L. & Pratt, R.G., 2004. Efficient waveform inversion and imaging: a strategy for selecting temporal frequencies, *Geophysics,* **69**(1), 231–248.

Tarantola, A., 1987, *Inverse Problem Theory: Methods for Data Fitting and Model Parameter Estimation,* Elsevier, New York.

Toulopoulos, I. & Ekaterinaris, J.A., 2006. High-order discontinuous Galerkin discretizations for computational aeroacoustics in complex domains, *AIAA J.,* **44,** 502–511.

Virieux, J., 1986. P-SV wave propagation in heterogeneous media, velocity-stress finite difference method, *Geophysics,* **51,** 889–901.

Zienkiewicz, O.C., Taylor, R.L. & Zhu, J.Z., 2005, *The Finite Element Method its Basis and Fundamentals,* 6th edn, Elsevier, London.

APPENDIX A: LAGRANGIAN BASIS FUNCTIONS

For the definition of the Lagrangian basis functions, the barycentric or tetrahedral coordinates $(\zeta_1, \zeta_2, \zeta_3, \zeta_4)$ that are linked to the cartesian coordinates (x, y, z) are defined inside an element as follows:

$$\begin{pmatrix} 1 \\ x \\ y \\ z \end{pmatrix} = \begin{pmatrix} 1 & 1 & 1 & 1 \\ x_1 & x_2 & x_3 & x_4 \\ y_1 & y_2 & y_3 & y_4 \\ z_1 & z_2 & z_3 & z_4 \end{pmatrix} \begin{pmatrix} \zeta_1 \\ \zeta_2 \\ \zeta_3 \\ \zeta_4 \end{pmatrix},$$

where (x_j, y_j, z_j) are the coordinates of the jth node of the element. Then, the Lagrangian basis functions can be defined with a linear combination of the tetrahedral coordinates depending on the approximation order. Following the node numbering convention given in Fig. 1, these functions are given by for the P_0 interpolation

$$\varphi_1 = 1,$$

for the P_1 interpolation

$$\varphi_1 = \zeta_1 \qquad \varphi_2 = \zeta_2 \qquad \varphi_3 = \zeta_3 \qquad \varphi_4 = \zeta_4,$$

and for the P_2 interpolation

$$\varphi_1 = (2\zeta_1 - 1)\zeta_1 \qquad \varphi_2 = (2\zeta_2 - 1)\zeta_2 \qquad \varphi_3 = (2\zeta_3 - 1)\zeta_3 \qquad \varphi_4 = (2\zeta_4 - 1)\zeta_4$$

$$\varphi_5 = 4\zeta_1\zeta_2 \qquad \varphi_6 = 4\zeta_1\zeta_3 \qquad \varphi_7 = 4\zeta_1\zeta_4 \qquad \varphi_8 = 4\zeta_3\zeta_2 \qquad \varphi_9 = 4\zeta_3\zeta_4 \qquad \varphi_{10} = 4\zeta_2\zeta_4.$$

APPENDIX B: MATRICES USED IN THE DG-FEM FORMULATION

$\mathcal{M}_\theta$ and $\mathcal{N}_\theta$ are constant real matrices defined by

$$\mathcal{M}_x = \begin{pmatrix} 1 & 1 & 0 & 0 & 0 & 0 \\ 0 & 0 & 0 & 1 & 0 & 0 \\ 0 & 0 & 0 & 0 & 1 & 0 \end{pmatrix} \qquad \mathcal{N}_x = \begin{pmatrix} 1 & 2 & -1 & 0 & 0 & 0 \\ 0 & 0 & 0 & 1 & 0 & 0 \\ 0 & 0 & 0 & 0 & 1 & 0 \end{pmatrix}^T$$

$$\mathcal{M}_y = \begin{pmatrix} 0 & 0 & 0 & 1 & 0 & 0 \\ 1 & 0 & 1 & 0 & 0 & 0 \\ 0 & 0 & 0 & 0 & 0 & 1 \end{pmatrix} \qquad \mathcal{N}_y = \begin{pmatrix} 0 & 0 & 0 & 1 & 0 & 0 \\ 1 & -1 & 2 & 0 & 0 & 0 \\ 0 & 0 & 0 & 0 & 0 & 1 \end{pmatrix}^T$$

$$\mathcal{M}_z = \begin{pmatrix} 0 & 0 & 0 & 0 & 1 & 0 \\ 0 & 0 & 0 & 0 & 0 & 1 \\ 1 & -1 & -1 & 0 & 0 & 0 \end{pmatrix} \qquad \mathcal{N}_z = \begin{pmatrix} 0 & 0 & 0 & 0 & 1 & 0 \\ 0 & 0 & 0 & 0 & 0 & 1 \\ 1 & -1 & -1 & 0 & 0 & 0 \end{pmatrix}^T.$$

For P_k, with $k \leq 2$, the volume integral in eqs (9) and (10) can be computed with the 11 Gauss points integration rule for tetrahedra (Keast 1986) and the surface integral in eqs (11) and (12) can be computed with the six Gauss points integration rule for triangles (Dunavant 1985).

Below, we give the expression of the matrices relevant for P_1 elements following the node numbering convention given in Fig. 1(b).

$$\mathcal{K}_i = \frac{vol_i}{20} \begin{pmatrix} 2 & 1 & 1 & 1 \\ 1 & 2 & 1 & 1 \\ 1 & 1 & 2 & 1 \\ 1 & 1 & 1 & 2 \end{pmatrix}, \tag{B1}$$

with vol_i as the volume of element i.

$$\mathcal{E}_{i\theta} = \frac{1}{12} \begin{pmatrix} S_{i1}n_{i1_\theta} & S_{i1}n_{i1_\theta} & S_{i1}n_{i1_\theta} & S_{i1}n_{i1_\theta} \\ S_{i2}n_{i2_\theta} & S_{i2}n_{i2_\theta} & S_{i2}n_{i2_\theta} & S_{i2}n_{i2_\theta} \\ S_{i3}n_{i3_\theta} & S_{i3}n_{i3_\theta} & S_{i3}n_{i3_\theta} & S_{i3}n_{i3_\theta} \\ S_{i4}n_{i4_\theta} & S_{i4}n_{i4_\theta} & S_{i4}n_{i4_\theta} & S_{i4}n_{i4_\theta} \end{pmatrix} \qquad \forall \theta \in \{x, y, z\}, \tag{B2}$$

with S_{ik} the surface of the face opposite to the kth node of element i and $\vec{n}_{ik} = (n_{ik_x}, n_{ik_y}, n_{ik_z})^T$ as the outward pointing unit normal vector with respect to the surface S_{ik}. For the computation of the flux matrices, we adopt a specific node numbering scheme. First, the neighbour element k is given by the node number of element i which is not shared between elements i and k. For instance, in Fig. 1(b), the neighbour element $k = 1$ is the element sharing the face (234) of element i. Second, the neighbour element nodes share the same node numbers of element i on the common face. Therefore, the opposite nodes of element i and k have also the same number. With this node numbering scheme, $\mathcal{F}_{ik}$ and $\mathcal{G}_{ik}$ are identical when both elements are P_1. We use this property to perform an efficient computation of the flux. In that case, we get

$$\mathcal{F}_{i1} = \frac{S_{i1}}{12} \begin{pmatrix} 0 & 0 & 0 & 0 \\ 0 & 2 & 1 & 1 \\ 0 & 1 & 2 & 1 \\ 0 & 1 & 1 & 2 \end{pmatrix} \qquad \mathcal{F}_{i2} = \frac{S_{i2}}{12} \begin{pmatrix} 2 & 0 & 1 & 1 \\ 0 & 0 & 0 & 0 \\ 1 & 0 & 2 & 1 \\ 1 & 0 & 1 & 2 \end{pmatrix}$$

$$\mathcal{F}_{i3} = \frac{S_{i3}}{12} \begin{pmatrix} 2 & 1 & 0 & 1 \\ 1 & 2 & 0 & 1 \\ 0 & 0 & 0 & 0 \\ 1 & 1 & 0 & 2 \end{pmatrix} \qquad \mathcal{F}_{i4} = \frac{S_{i4}}{12} \begin{pmatrix} 2 & 1 & 1 & 0 \\ 1 & 2 & 1 & 0 \\ 1 & 1 & 2 & 0 \\ 0 & 0 & 0 & 0 \end{pmatrix}. \tag{B3}$$